

Modelling and Analysis of Semiconductor Lasers Under Fiber Bragg Grating Feedback

J. Steele,^{1,2,*} B. Krauskopf,^{1,2} and N. Broderick^{1,3}

¹*Dodd-Walls Centre for Photonic and Quantum Technologies, New Zealand*

²*Department of Mathematics, University of Auckland, New Zealand*

³*Department of Physics, University of Auckland, New Zealand*

(Dated: September 9, 2025)

Semiconductor lasers are compact, efficient light sources widely used in optical communications, and their sensitivity to external feedback makes them rich systems for studying nonlinear dynamics. The Lang-Kobayashi (LK) equations are the standard tool for modelling lasers subject to external feedback from a regular mirror. A key reflective component in optical systems is the fiber Bragg grating (FBG)—a periodic optical fiber refractive index variation—leveraged for its precise spectral control and all-fiber compatibility. When the external feedback comes from an FBG, present modelling requires a computationally expensive convolution term, which provides limited analytical insight into the system’s behaviour. We present a novel modelling approach that approximates FBG feedback by a sum of discrete delay terms. Critically, this avoids the need for numerical convolution while preserving the essential physics. This enables detailed analysis of the laser’s mode structure, stability regimes, and bifurcation structure in the spirit of that for the ‘classic’ LK equations. In this way, our work provides a foundation for deeper theoretical study of semiconductor lasers subject to technologically relevant types of FBG feedback, bridging the gap between numerical simulation and analytical understanding.

I. INTRODUCTION

Semiconductor lasers are fundamental components in modern photonic technologies. Their emission wavelengths align with those used in optical communication networks, making them valuable light sources. In addition, they are orders of magnitude smaller than typical helium–neon lasers, with coherence lengths of only a few millimetres compared to many metres, which enables widespread practical applications [1]. Semiconductor lasers are not only smaller than conventional gas lasers, but also exhibit much higher output coupling, with approximately 70% of the light intensity escaping them compared to 1–5% for gas lasers [2]. However, this openness makes semiconductor lasers more susceptible to external disturbances, leading to a strong response to incident signals. Although undesirable in practical applications, this sensitivity has made semiconductor lasers a central platform for investigating nonlinear dynamics induced by external optical feedback. The influence of external light on laser operation has been extensively investigated since the 1970s, with particular focus on conventional optical feedback (COF), typically achieved by reflecting output laser light back into the laser cavity using a mirror, as well as on optical injection of laser light from another laser [3]. Feedback and injection mechanisms have important practical implications: for example, the former arises in the operation of CD players, while the latter is central to laser amplification systems. Beyond their direct historical significance, semiconductor lasers with feedback underpin key technologies in modern photonics. Feedback control is exploited to stabilize

frequency and linewidth in coherent optical communication [4], to enhance sensitivity in precision sensing and metrology, and to enable secure chaos-based encryption schemes [5]. At the same time, semiconductor lasers with feedback provide a prototypical and experimentally accessible example of delay differential equations (DDEs), serving as a testbed for nonlinear dynamics with relevance extending to control theory [6], electronics, and biological systems [7].

A. Lang-Kobayashi equations

A major breakthrough occurred in 1980 with the seminal work of Lang and Kobayashi, who introduced the Lang–Kobayashi (LK) rate equations to describe the dynamics of a semiconductor laser subject to COF from a distant external mirror [8]. The LK equations describe the time evolution of the complex electric field $E = E_x + iE_y$ and the carrier inversion N under the influence of external feedback $F(t)$. A nondimensionalized form of these equations, highlighting the key parameters governing the system dynamics, is given by (1) [9]

$$\begin{aligned} \frac{dE}{dt} &= (1 + i\alpha)N(t)E(t) + \eta F(t) \\ T \frac{dN}{dt} &= P - N(t) - (1 + 2N(t))|E(t)|^2 \end{aligned} \quad (1)$$

where $F(t) = e^{-i\omega_0\tau}E(t - \tau)$. These key parameters can be separated into intrinsic laser parameters and external cavity (EC) parameters. The laser, emitting at a single frequency ω_0 , is characterised by the pump current P , the linewidth enhancement factor α , and the ratio of photon and electron decay times $T = \tau_e/\tau_p$. The EC is characterised by the round-trip delay time $\tau = 2L_{\text{EC}}/c$, the feedback power level (defined as the ratio of power

* jste924@aucklanduni.ac.nz

reflected from the external mirror to that from the diode mirror) η , and the feedback phase $C_p = \omega_0 \tau$, corresponding to the number of optical wavelengths in the EC. The application of these equations requires a single-mode laser subject to weak feedback (up to a few percent of the emitted light) from a long EC ($\mathcal{O}(\text{cm})$ – $\mathcal{O}(\text{m})$). As the LK equations assume single-mode operation, they do not capture mode competition or spectral dynamics; for approaches to the analysis of multimode lasers, see [10] and references therein. A long EC justifies treating the feedback phase C_p as an independent parameter from the delay τ , since a 2π phase shift corresponds to only a half-wavelength change (about one micron), which is negligible at these scales [11]. In practice, varying C_p over a full 2π is achieved by shifting the mirror position by less than a micron for visible wavelengths, for example using a piezoelectric transducer [9]. It is noted that, these equations are formulated with reference to the centre frequency of the laser, with $\omega_0 = 0$ at the operating frequency, which implies $C_p = 0$ in the first instance. The weak-feedback condition further ensures that multiple EC reflections between the laser facet and the external mirror can be neglected; if this condition is not satisfied, the feedback $F(t)$ takes a more complex form [2].

$$F(t) = \frac{r_2^2 - 1}{r_2^2} \sum_{n=1}^{\infty} (-r_2 r)^n e^{-inC_p} E(t - n\tau) \quad (2)$$

The LK equations successfully capture the rich dynamical behaviour of semiconductor lasers under weak external feedback, including steady-state, periodic, quasi-periodic, and chaotic emission, as well as complex behaviours such as regular pulse packages (RPPs), coherence collapse (CC), and low-frequency fluctuations (LFFs) [12]. The delay $E(t - \tau)$ present in the feedback term $F(t)$ makes the LK equations DDEs with phase space in the infinite-dimensional Banach space $C([- \tau, 0], \mathbb{C} \times \mathbb{R})$, consisting of continuous functions that describe the past history of the optical field. Due to the rotational symmetry of the complex field E , the effective phase space is this function space modulo the action of S^1 . This memory effect, arising from time-delayed optical feedback whereby the system evolves according to both its current and past states, is absent in injected semiconductor laser systems, where dynamics are instead dominated by phase-locking and frequency pulling [13, 14]. The impact of the LK equations stems from their role as a minimal yet sufficient model: a coupled nonlinear DDE system that reproduces experimentally observed behaviours while remaining amenable to rigorous analysis. In this framework, equilibria can be analysed in detail, including their creation and annihilation via saddle-node bifurcations and their loss of stability through Hopf bifurcations, yielding a clear picture of local dynamics [15]. Moreover, numerical continuation tools for DDEs, such as `DDE-Biftool`, enable systematic tracking of equilibria and periodic orbits, as well as the detection of sec-

ondary bifurcations that organise the global dynamics [16, 17].

A central insight of the LK model is the structure of its steady states, known as external cavity modes (ECMs). The ECMs form an ellipse in frequency space centred at the free-running laser frequency, with the maximum gain mode (MGM) located on the outer boundary, farthest from the centre frequency. The number of ECMs and the frequency interval they occupy increase with feedback strength and external cavity length. ECMs are typically created in saddle-node pairs as parameters vary, and their stability changes through Hopf bifurcations [9, 15]. The set of ECMs provides the backbone of the LK dynamics: it organises transients and families of periodic and quasi-periodic motions that arise from Hopf and subsequent bifurcations. In regimes such as LFFs and CC, trajectories spend long intervals near weakly stable ECMs before departing along unstable manifolds of neighbouring saddle ECMs, producing intensity dropouts; the prevalence and severity of these behaviours increase with the size of the ECM ellipse [9, 17]. Thus, understanding the geometry, multiplicity, and stability of ECMs is essential for explaining observed dynamical regimes and for devising control strategies. This perspective naturally motivates efforts to reduce or confine the set of accessible ECMs, thereby enhancing stability under stronger feedback by limiting the number of available steady-states. A crucial step in this direction is understanding how different forms of feedback, beyond conventional optical feedback, can suppress or restructure the ECM ellipse, providing new routes to controlled laser dynamics.

Phase-conjugate feedback

A single-mode semiconductor laser with phase-conjugate feedback (PCF) receives wavefront-inverted light from a phase-conjugating mirror (PCM), typically realised by degenerate four-wave mixing in vapours or semiconductors or by gratings and optical crystals, creating a self-aligning configuration that compensates EC distortions. By reversing wavefront errors on each round trip, phase conjugation stabilises both beam quality and frequency, motivating its application in semiconductor lasers. Owing to these potential stabilisation features, PCF was among the earliest feedback configurations investigated beyond COF [18, 19]. In the standard LK rate-equation framework (1), PCF is represented by a delayed conjugated field term, $F(t) = e^{-i\phi_{\text{PCM}}} E^*(t - \tau)$, which yields a DDE system with discrete \mathbb{Z}_2 symmetry $E \rightarrow -E$ [20]. This symmetry leads to qualitative differences in the mode structure: whereas COF produces a continuous ellipse of ECMs organised by the feedback phase, PCF gives rise instead to isolated branches of pulsating ECMs whose frequencies are locked near integer multiples of the cavity frequency [21]. Within the locking range, the PCF laser is both frequency- and phase-locked to the pump, and, unlike COF, phase locking does

not depend on the feedback phase. Overall, the resulting linewidth is ultranarrow and robust against added noise [22].

Filtered optical feedback

The most direct method of controlling the ECMs in a semiconductor laser is to filter the light fed back into the cavity, a scheme known as filtered optical feedback (FOF). By modifying the spectrum of the reinjected light, FOF reshapes the set of accessible ECMs. Several practical implementations of FOF have been investigated. One approach is the insertion of a Fabry–Pérot resonator within the feedback loop [23]. More commonly, the external mirror is replaced by a frequency-selective surface, such as a grating [24–26], or by a phase-conjugating surface, for example a Kerr-type nonlinear medium, which in this context acts primarily as a spectral filter [27]. As expected, all of these implementations lead to significant linewidth narrowing, resulting in more stable operation around the filter’s free-running frequency. This makes FOF a practical approach for stabilising single-mode operation and narrowing emission spectra in photonic applications.

Mathematical analysis of FOF poses additional challenges. In this case, the spectral components of the electric field must be included explicitly, since their reflection is governed by the frequency response of the chosen filter, denoted $\rho(\omega)$. Therefore, the feedback term $F(t)$ must be replaced by a more general expression that accounts for this frequency selectivity. For a given reflection response, $F(t)$ can be obtained by decomposing the field into its Fourier components, applying the filter’s reflectivity spectrum $\rho(\omega)$, and then taking the inverse Fourier transform [28]. Mathematically, this amounts to

$$\begin{aligned} F(t) &= \mathcal{F}^{-1}[\mathcal{F}[E(t)](\omega) \times \rho(\omega)](t - \tau) \\ &= \frac{1}{2\pi} \int_{-\infty}^{\infty} \rho(\omega) \int_{-\infty}^{\infty} E(t') e^{-i\omega t'} dt' e^{i\omega(t-\tau)} d\omega. \end{aligned} \quad (3)$$

This expression highlights that the feedback is no longer a simple delayed replica of the field, but a spectrally filtered version shaped by $\rho(\omega)$. Unlike COF and PCF, FOF directly reshapes the spectral window of accessible ECMs. Note that (3) again assumes a single reflection is sufficient to describe the external feedback signal $\eta F(t)$. The distributed nature of the feedback expressed in (3) makes the system difficult to treat analytically and computationally demanding to simulate. The modified LK equations take the form of integro-differential equations that are not amenable to standard bifurcation analysis tools, such as fixed-point calculation and stability analysis, which obscures even basic insights into the influence of filtering on the system. Furthermore, numerical methods such as direct time-series integration of (E, N) become significantly more computationally demanding, since (3) must be re-evaluated at every time step through

numerical integration, rather than simply retrieving the stored value $E(t - \tau)$ as in the standard LK equations.

A key insight was provided in 1999 by Yousefi and Lenstra [28], who assumed that filtering yields a frequency-dependent reflectivity spectrum $\rho(\omega)$ represented as a sum of Lorentzians. By considering a single Lorentzian, which can adequately describe certain external feedback mechanisms [23, 24], they showed that the integro-differential equations for distributed FOF can be reduced to a system of DDEs. In this formulation, the first two equations remain identical to the standard LK system, while the effect of filtering is incorporated by coupling an additional equation for $F(t)$.

$$\frac{dF}{dt} = \Lambda E(t - \tau) e^{-iC_p} + (i\Delta - \Lambda) F(t) \quad (4)$$

Here, Λ is the full width at half maximum (FWHM) of the filter, which sets its spectral width, and Δ is the detuning of the Lorentzian filter from the laser’s free-running frequency. Since coupling (4) to the standard LK equations (1) again yields a system of DDEs, the model remains amenable to the same analytical and numerical methods as the original LK system. They demonstrated that, as expected, the system generally admits fewer ECMs than COF and that, overall, filtering leads to more stable dynamics. Alongside the reduction in the number of accessible ECMs, the MGM tends to lie closer to the filter frequency (though not exactly at it) rather than at the edge of the fixed-point ellipse as in COF. Overall, the formulation of these equations as coupled DDEs allows for detailed investigation through continuation and stability analysis of the stationary states, providing deeper insight into the influence of FOF on semiconductor lasers [11, 29–39].

Fiber Bragg grating feedback

Fiber Bragg gratings

One frequency-selective component that has been the focus of extensive research in recent decades is the fiber Bragg grating (FBG). FBGs offer several advantages over other fibre-optic technologies. These include all-fibre design, low insertion loss, high return loss, potential for lower cost, and, most notably, exceptional flexibility in tailoring spectral characteristics. With current manufacturing techniques, gratings can be fabricated with nearly arbitrary spectral responses $\rho_{\text{Bragg}}(\omega)$ and normalised bandwidths ranging from 10^{-4} to 0.1 [40]. The FBG is therefore a natural reflective element for implementing FOF.

An FBG is defined as a periodic modulation $\delta n_{\text{eff}}(z)$ of the refractive index with period Λ along a fibre of length L_{FBG} . The number of gratings in an FBG is therefore $N = L_{\text{FBG}}/\Lambda$. The most general form of this

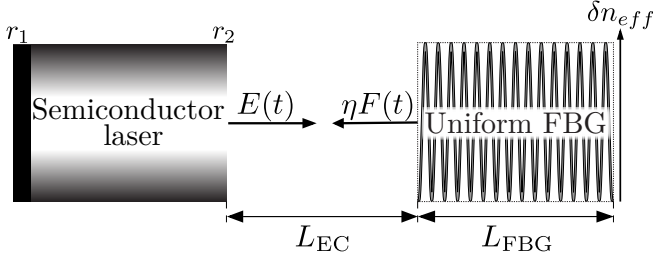


FIG. 1. Sketch of an optical fiber with an FBG written along its length.

periodic modulation is

$$\delta n_{eff}(z) = \overline{\delta n_{eff}}(z) \left[1 + v \cos \left(\frac{2\pi}{\Lambda} z + \phi(z) \right) \right]. \quad (5)$$

Here, $\overline{\delta n_{eff}}(z)$ describes the envelope of the periodic modulation along L_{FBG} ; for example, $\overline{\delta n_{eff}}(z) \sim e^{-z^2}$ yields a Gaussian refractive index profile. This flexibility allows tailoring of the spectral response through modulation depth and phase, directly influencing the accessible ECM structure. In addition to the envelope, v denotes the fringe visibility of the index modulation, and $\phi(z)$ allows variation of the grating period along the fibre, enabling different frequencies to be reflected at different positions.

Light propagating in the fibre and interacting with the FBG undergoes diffraction when its wavelength is close to the design wavelength, $\lambda_D = 2n_{eff}\Lambda$. It is typically assumed that the light undergoes only first-order diffraction, which dominates in FBGs, so that a single propagating mode is considered; higher-order diffraction is negligible under standard design conditions. In this case, using coupled-mode theory and the synchronous approximation, one can derive coupled first-order differential equations describing the interaction between the forward- and backward-propagating waves, $A(z)$ and $B(z)$, respectively. For further details, see [40] and references therein.

$$\begin{aligned} \frac{dR}{dz} &= i\hat{\sigma}R(z) + i\kappa S(z), \\ -\frac{dS}{dz} &= i\hat{\sigma}S(z) + i\kappa R(z), \end{aligned} \quad (6)$$

with $R(z) = A(z) \exp(-i(\phi/2 - \delta z))$, $S(z) = B(z) \exp(-i(\phi/2 + \delta z))$. The parameters δ , the wavevector mismatch, κ , the alternating-current (AC) coupling coefficient, and $\hat{\sigma}$, the direct-current (DC) self-coupling coefficient, are given by

$$\delta = 2\pi n_{eff} \left(\frac{1}{\lambda} - \frac{1}{\lambda_D} \right) \quad (7)$$

$$\kappa = \frac{\pi}{\lambda} v \overline{\delta n_{eff}}(z) \quad (8)$$

$$\hat{\sigma} = \frac{2\kappa}{v} + \delta - \frac{1}{2} \frac{d\phi}{dz} \quad (9)$$

Since κ and $\hat{\sigma}$ generally depend on z , (6) cannot in general be solved analytically, but they can be readily solved numerically once Λ , n_{eff} , $\overline{\delta n_{eff}}(z)$, $\phi(z)$, and L_{FBG} are specified.

At this point, all the necessary ingredients are in place to calculate the key characteristic of an FBG—its reflectivity spectrum $\rho(\omega)$. Physically, the primary interest lies in the reflection spectrum of light reflected at the front FBG interface, assuming no reflection from the back interface. Therefore, (6) is typically solved by setting $z = 0$ at the midpoint of the FBG, imposing boundary conditions $R(-L_{FBG}/2) = 1$ and $S(L_{FBG}/2) = 0$, and integrating backwards from $L_{FBG}/2$ to $-L_{FBG}/2$. The amplitude reflection coefficient is then given by

$$\rho = \frac{S(-L_{FBG}/2)}{R(-L_{FBG}/2)} \quad (10)$$

which defines the reflectivity spectrum $\rho(\omega)$. Although (6) must generally be solved numerically and closed-form expressions for $\rho(\omega)$ are rarely available, certain standard grating designs such as uniform or raised-cosine-apodised gratings admit analytic solutions and provide valuable insight into the typical properties of FBG reflection spectra. Among the different grating profiles, the simplest and most widely studied is the uniform grating.

Uniform FBG reflection spectra $\rho_{Bragg}(\omega)$

The uniform FBG serves as the canonical case for analysis, characterised by constant period and constant modulation depth. It admits analytic solutions that not only reveal the fundamental characteristics of FBG reflection spectra but also serve as a reference for more complex grating designs. In this case, the grating chirp satisfies $d\phi/dz = 0$ and the apodisation is constant, $\overline{\delta n_{eff}} = \text{const.}$, so that the grating index variation given by (5) reduces to a sine wave, as shown in Figure 1. Therefore, κ and $\hat{\sigma}$ are constant in z , which allows the reflectivity spectrum $\rho(\omega)$ to be obtained analytically by solving (6) and then evaluating (10).

$$\rho = \frac{-\kappa \sinh(L_{FBG})}{\hat{\sigma} \sinh(\gamma L_{FBG}) + i\gamma \cosh(\gamma L_{FBG})} \quad (11)$$

where $\gamma = \sqrt{\kappa^2 - \hat{\sigma}^2}$. Several key features of the reflection spectrum $\rho(\omega)$ are most clearly visualised by plotting it as a function of normalised frequency while varying κL_{FBG} for a fixed N [40].

$$\frac{\omega}{\omega_{\max}} = 1 + \frac{\hat{\sigma} L_{FBG}}{\pi N}$$

Figure 2 shows representative amplitude reflectivity and phase spectra for uniform gratings, plotted against angular frequency. The gratings are centred at the common laser wavelength of 1550 nm, with $\kappa L_{FBG} \in 0.5, 2, 5$ and a fixed $N = 5000$, chosen to illustrate weak, moderate, and

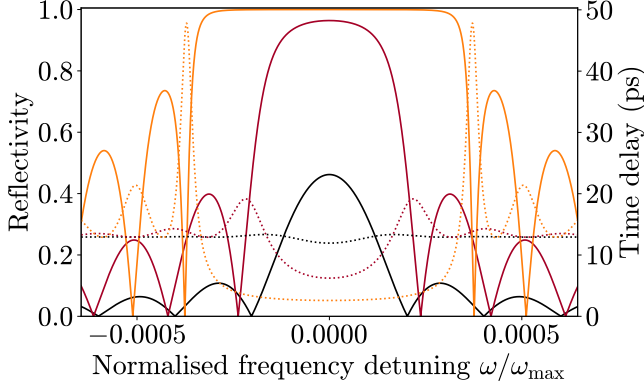


FIG. 2. Examples of magnitude and phase of uniform FBG reflection spectra with varying dimensionless grating strength $\kappa L_{\text{FBG}} \in [0.5, 2, 5]$ and constant number of grating periods $N = 5000$.

strong coupling regimes. Increasing N (and thus L_{FBG}) results in a narrower reflection bandwidth, whereas decreasing N (and thus L_{FBG}) produces a broader one, provided that κL_{FBG} remains constant. The reflection spectrum consists of a main lobe and a series of side lobes, separated by reflection zeros that are symmetrically spaced in wavelength on either side of the main lobe. For gratings with low κL_{FBG} , such as 0.5, the main lobe has a bandwidth, defined as the interval between its reflection zeros, that is twice the width of the side lobes [40]. Evidently, increasing κL_{FBG} increases the grating's maximum reflectivity and also broadens the main-lobe bandwidth while narrowing that of the side lobes. Additionally, the time delay is approximately constant for low reflectivities but becomes increasingly distorted as κL_{FBG} increases.

Since κ and $\hat{\sigma}$ depend only on λ and the prescribed grating parameters, the reflected amplitude $|\rho|$ and phase $\arg(\rho)$ can be directly plotted against frequency by substituting (8) and (9) into (11). Figure ?? shows examples of reflection spectra of uniform FBGs plotted against frequency, with the design frequency given by

$$\omega_D = \frac{\pi c}{\Lambda n_{eff}^2} \quad (12)$$

highlighted to demonstrate the intrinsic frequency shift in the spectrum. The reflection spectrum of a uniform grating has a maximum reflectivity

$$R \equiv |\rho_{\text{max}}| = \tanh(\kappa L_{\text{FBG}}) \quad (13)$$

centred at the Bragg frequency ω_{max} ,

$$\omega_{\text{max}} = \frac{\omega_D}{\left(1 + \frac{\delta n_{eff}}{n_{eff}}\right)} \quad (14)$$

corresponding to the peak reflectivity. We note that R is more commonly used to denote reflected power rather than reflected amplitude; however, the present notation

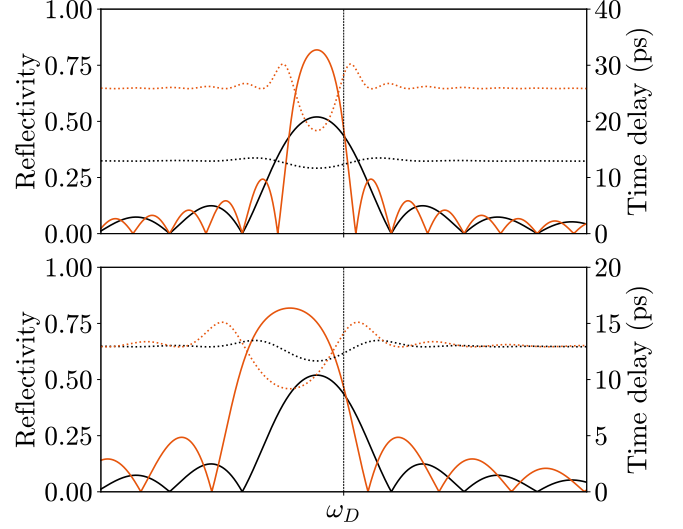


FIG. 3. Examples of the magnitude and group delay of uniform FBG reflection spectra, illustrating the effect of varying δn_{eff} and L_{FBG} . The nominal case (black curves) corresponds to $\delta n_{eff} = 5 \times 10^{-5} n_{eff}$ and $L_{\text{FBG}} = 2.64$ mm; in (a) the grating length is doubled to $L_{\text{FBG}} = 5.28$ mm, and in (b) the index change is doubled to $\delta n_{eff} = 1 \times 10^{-4} n_{eff}$.

is adopted for clarity in later sections. The phase at ω_{max} is $\pi/2$ for all uniform gratings, while the reflection zeros are symmetric about ω_{max} . The first zeros on either side of the main lobe occur at $\omega_{\text{max}} \pm \omega_z$, where

$$\omega_z = \omega_{\text{max}} \sqrt{\left(\frac{\delta n_{eff}}{2n_{eff}}\right)^2 + \frac{1}{N^2}} \quad (15)$$

and the phase of the reflection spectrum shifts by 2π between these zeros. Outside the main lobe, the reflectivity peaks of the side lobes decay exponentially, with a π phase change across each lobe.

Figure 3(a) shows that doubling L_{FBG} increases R because more grating periods contribute to reflection, reducing transmission. At the same time, the bandwidth of each lobe is halved, while the offset from the design frequency remains unchanged. In contrast, doubling δn_{eff} , as shown in (b), again increases R , but now the offset from the design frequency increases while the bandwidth remains unchanged. Since these two parameters govern the three key spectral features—offset, maximum reflectivity, and bandwidth—one cannot vary a single feature independently. Instead, compensation requires adjusting the grating period Λ , which shifts ω_{max} while leaving ω_z and R essentially unchanged. This holds because laser centre frequencies are in the THz range, whereas the frequency offset is at most in GHz, so $\omega_{\text{max}}/\omega_D = \Lambda_D/\Lambda_{\text{max}} \approx 1$. Using this approximation, together with (14) and (15), δn_{eff} , L_{FBG} , and Λ can be

calculated sequentially.

$$\bar{\delta n}_{eff} \approx \frac{2\omega_z}{\omega_c} \frac{n_{eff}}{\sqrt{1 + \left(\frac{\pi}{\operatorname{arctanh}(R)}\right)^2}} \quad (16)$$

$$\Lambda = \frac{\pi c}{\omega_c n_{eff} (n_{eff} + \bar{\delta n}_{eff})} \quad (17)$$

$$L = \frac{\Lambda}{\sqrt{\left(\frac{\omega_z}{\omega_c}\right)^2 - \left(\frac{\bar{\delta n}_{eff}}{2n_{eff}}\right)^2}} \quad (18)$$

For example, if a uniform grating with a spectral response corresponding to $\omega_c = 1.216 \times 10^{15} \text{ rad s}^{-1}$, $\omega_z = 1 \times 10^{10} \text{ rad s}^{-1}$, and $R = 0.5$ is desired, (16) provides grating parameters $\bar{\delta n}_{eff} = 4.2111838 \times 10^{-6}$, $\Lambda = 3.6494583 \times 10^{-7} \text{ m}$, $L = 0.0444578955 \text{ m}$, which gives excellent agreement to the desired spectral response as shown in Figure ??.

FBG DISTRIBUTED FEEDBACK

Given the significant spectral advantages of FBGs for FOF and the straight-forward integration of FBGs into fiber optic semiconductor laser systems, investigations into their influence on the dynamics of external feedback semiconductor laser systems is of great interest. A sketch of the laser system under external feedback from an FBG is shown in Figure ??. As demonstrated in the previous section, the reflectivity spectrum of FBGs can be rather complex. As an FBG in essence acts as a filter, the term $F(t)$ will be given by (3) with $\rho(\omega) = \rho_{\text{Bragg}}(\omega)$. This term can alternatively be written as a convolution in the time domain,

$$F(t) = e^{-iC_p} \tilde{\rho}_{\text{Bragg}}(t) \otimes E(t - \tau) \quad (19)$$

where $\tilde{\rho}_{\text{Bragg}}(t)$ is the impulse response of the FBG with respect to the Bragg resonance frequency. Analytic expressions do not exist for the impulse response, even for simple gratings, and must therefore be calculated numerically through fast Fourier transforms (FFTs), for example. The requirement of numerically calculating $F(t)$ limits the analysis to numerical integration of solutions for $(E(t), N(t))$, and calculating properties of resulting time series, such as maximal Lyapunov exponents (MLEs) or spectral characteristics such as signal dispersion. Despite the obvious computational and analytical difficulties associated with this feedback term, research has been conducted into uniform FBG feedback using the convolution representation for $F(t)$ [41–46]. In several studies, an expression for $\rho(\omega)$ separates the reflection spectrum and detuning, allowing the detuning to be varied continuously while keeping the reflectivity spectrum shape constant. In this case, the reflected signal has the form,

$$F(t) = \eta e^{-iC_p} [\tilde{\rho}_0(t) e^{i\omega_B t}] \otimes E(t - \tau)$$

where $\tilde{\rho}_0$ is centred at the laser free-running frequency, while the detuning ω_B is an independent parameter. Although this form for the reflectivity distribution allows one to vary a single feature of the reflectivity distribution, as discussed in ??, the detuning and distribution shape intrinsically depend on each other, meaning that all grating parameters $\bar{\delta n}_{eff}, \Lambda, L$ must be simultaneously adjusted in order to continuously detune over a constant distribution shape [46]. These parameters can be calculated for example through (16). Similarly, the distribution width and maximum reflectivity (occurring at ω_c) can only be independently varied through simultaneously varying all grating parameters.

As numerical investigations only allow limited insights into the underlying dynamics of FBG feedback, initial numerical investigations focused on the potential of FBG feedback to produce high-quality chaotic signals. This is of research interest as chaotic signals produced by lasers subject to external feedback are used in a number of applications such as high-speed optical random bit generation [5] and chaos-based secure communication [47]. It was demonstrated that FBG feedback is more effective than conventional mirror feedback in suppressing the time-delay signature (TDS) associated with chaos generation in semiconductor lasers. TDS can limit the encryption capabilities of chaotic signals generated lasers subject to external feedback, as powerful autocorrelation algorithms can use a signal's TDS to partially or fully decrypt the signal [48]. The improvement in TDS suppression was generally attributed to the time-distributed reflections provided by the FBG, 'spreading out' the effective time delay of the chaotic signal [41]. Further, it was observed that TDS suppression improves as the bandwidth of the FBG decreases. This is linked to the increase in dispersion of the reflection group delay, which plays a crucial role in the dynamics of the laser. Notably, the length of the FBG does not significantly affect this suppression. Although narrower FBG bandwidth enhances chaotic signal TDS suppression, the size of parameter regions that exhibit chaos decrease, being replaced by regions of stable period-1 periodic orbits, in agreement with analyses of FOF [43], although it was demonstrated that in some cases, chaos can be induced by FBG feedback for lower time delays than what is possible using COF. Further investigations showed that optimal TDS suppression is achieved when the FBG is positively detuned from the laser frequency. The preference for positive detuning is attributed to the red-shifting of the laser cavity due to the anti-guidance effect [42].

The convolution representation for $F(t)$ under FBG feedback can alternatively be written as a distributed delay term. Using the definition of the convolution,

$$\begin{aligned} \tilde{\rho}(t) \otimes E(t - \tau) &= \int_{-\infty}^{\infty} \tilde{\rho}(t - s) E(s - \tau) ds \\ &= \int_{-\infty}^{t+\tau} \tilde{\rho}(t - s) E(s - \tau) ds \end{aligned}$$

as $E(s - \tau) = 0$ for $s > t + \tau$. Now, choosing the lower

bound $t - T$ so that $\tilde{\rho}(s) \approx 0 \forall s > T$.

$$\tilde{\rho}(t) \otimes E(t - \tau) \approx \int_{t-T}^{t+\tau} \tilde{\rho}(t-s)E(s-\tau)ds$$

This equivalent expression for $F(t)$ has been used in further numerical studies on the use of chirped FBGs (CFBGs), which are of interest in TDS suppression due to their enhanced dispersion characteristics compared to the previously explored uniform FBGs [49–52]. An illustration of the index profile of CFBGs is given in Figure ??(d). As there are no analytic expressions for a chirped reflectivity spectrum compared to a uniform one, (6) must be solved numerically, further increasing computational complexity. The impulse response $\tilde{\rho}(t)$ involved in the distributed feedback is calculated through FFTs as done in previous investigations. Investigations into CFBG feedback demonstrated enhanced TDS compared to uniform FBG feedback, eliminating TDS without requiring amplification, simplifying system configuration.

More recently, investigations have gone beyond studying chaotic signal generation but similar to the previous analyses, the convolution representation for $F(t)$, restricted computations to basic time series generation. Sk nderaset *al.* observed that the location of the zeros of the reflectivity spectrum, can strongly influence laser stability. They demonstrated that these stability fluctuations are likely due the damping of relaxation oscillations (ROs) when the zeros of the FBG reflectivity spectrum is aligned with the laser’s RO frequency (ω_{RO}) side lobes. These stability fluctuations were found by tracking the required feedback rate to produce a Hopf bifurcation, that is, where constant intensity emission begins to periodically fluctuate, for increasing the FBG length which in turn decreases FBG bandwidth. As changing FBG length changes its reflectivity, the other FBG parameters are required to be adjusted to ensure a constant reflectivity. Asymmetry in stability fluctuations were observed for frequency detuning relative to the Bragg wavelength, as was the case in previous studies [41], but alternatively attributed to the frequency-dependent phase shift induced by the FBG [45, 46]. This gives further indication that the observed asymmetrical behaviour with respect to detuning emerges as an intrinsic characteristic of FBG feedback. Overall, the numerical simulations reveal that FBG feedback shares many features with FOF. However, the precise shape, location of reflection zeros, and, most notably, the phase of the FBG introduce additional complexity.

While the representation of $F(t)$ as a convolution has been shown to provide some limited insights into FBG feedback, an alternative form for $F(t)$ has been shown to allow deeper analyses into its associated dynamics. The case of FBG feedback subject to strong feedback was considered in a series of papers by Naumenko *et al.* [53–55]. The modified rate equations used in the analysis are based on a model first proposed in 1989 [56] describing strong feedback due to a plain mirror. They replace the feedback term $\eta e^{-iC_p} E(t - \tau)$ in the LK rate equations

with the term $E(t) \ln [E_r(t)/E(t)]$ where $E_r(t)$ accounts for the multiple EC reflections caused by the strong COF, similar to (2) by defining

$$E_r(t) = E(t) + \frac{R_2^2 - 1}{R_2^2} \sum_{n=1}^{\infty} (-R_2 R)^n e^{-inC_p} E(t - n\tau)$$

Indeed, truncating this expression for $F(t)$ to first order reduces to single reflection feedback. Taking the Taylor expansion of the logarithm,

$$\begin{aligned} E(t) \ln \left[\frac{E_r(t)}{E(t)} \right] &= \sum_{n=1}^{\infty} \frac{(-1)^{n-1}}{n} \left(\frac{E_r(t)}{E(t)} - 1 \right)^n \\ &\stackrel{n=1}{\approx} E(t) \left(\frac{E(t) + \frac{R_2^2 - 1}{R_2^2} (-R_2 R) e^{-iC_p} E(t - \tau) - E(t)}{E(t)} \right) \\ &= \eta e^{-iC_p} E(t - \tau) \end{aligned}$$

as desired. Reflection due to an FBG can be modelled by modifying this expression to account for the spectral filtering $\rho_{\text{Bragg}}(\omega)$ of the grating. Multiple reflections given by the terms $(R_2 R)^n e^{-inC_p} E(t - n\tau)$ are now replaced by terms given by (3), see Appendix C for details. Through the use of Green’s functions, an expression for the ECMs of the system can be derived, allowing for significantly deeper insights into the dynamics compared to the convolution method discussed previously. It was shown that under weak feedback, the stationary ECM states are mostly confined to the main lobe of the gratings reflectivity spectrum, while the MGM is shifted close to $\omega_B = 0$, identical to the results presented by Yousefi and Lenstra in the case of FOF. They additionally identified ‘satellite’ ECMs, for narrow bandwidth FBGs, separated from the central ECM ellipse by the zeros of the main lobe. It is shown that under strong feedback conditions that narrow filters lead to the excitation of additional solutions confined to the side lobes of the FBG frequency response. Although numerical integration of the presented system can be performed, and stationary states calculated, the complexity of $F(t)$ prevents the use of advanced bifurcation tools such as numerical continuation and stability analysis of the stationary solutions, clouding the underlying dynamics induced by the frequency-dependent FBG reflection.

The similarities in the results of Naumenko *et al.* to work on FOF is fairly evident when one considers a single reflection. Carrying out the same first-order approximation on this feedback term yields an equivalent feedback term as used in the original FOF definition considered by Yousefi and Lenstra with $\rho(\omega) = \rho_{\text{Bragg}}(\omega)$. See Appendix C for further details. Therefore, it is natural to ask if there is a an approximation to $\rho_{\text{Bragg}}(\omega)$ which captures its key frequency-dependent reflection effects while enabling the feedback term $\eta F(t)$ to be reduced to DDEs which amenable to advanced bifurcation analysis.

II. UNIFORM FBG MODELLING THROUGH DISCRETISED REFLECTIONS

Although all research in the literature up to this point on the modelling of FBG feedback has had as its starting point the gratings spectral response, there has been success in modelling FBGs by considering the discretised reflections that occur within the grating during the distributed feedback. This is essentially a discretised version of the time dependent impulse response $\tilde{\rho}(t)$. Note that where the impulse response is written explicitly in the feedback term $F(t)$, it is obtained through $\rho(\omega)$ by an inverse Fourier transform. By considering all paths that emerge back out of the FBG after a given time delay $N\delta\tau$, that is, all paths that have undergone reflections in N layers (with each layer having the same round trip time), one can force the impulse response of the structure to be formed by a sum of delta functions,

$$\tilde{\rho}(t) = \sum_{k=0}^N h_r(k) \text{Dirac}(t - \tau - k\delta\tau) \quad (20)$$

where $h_r(k)$ is the effective reflection coefficient for light that has propagated through k layers. Figure 4(a) provides an illustration of the discretised reflections. For many gratings, the average refractive index changes over the grating length, see Figure ??(b), for example. Therefore, a different refractive index n_i for each layer and therefore, different layer-to-layer transmission and reflection coefficients, $t_{i,i+1}$ and $r_{i,i+1}$ must be calculated. This method has been demonstrated to accurately recover the spectral response $\rho(\omega)$ [57]. We note this form can be used to represent the feedback term $F(t)$ without considering the spectral effects of the FBG itself, once the coefficients $h_r(k)$ have been determined.

In the past, all intra-layer reflections have been considered and summed over to produce expressions for the total reflection after a time delay $k\delta\tau$ [58]. We consider a simpler model, initially applied to uniform FBGs whose average refractive index remains constant over the grating length. We demonstrate has the benefits of the mathematical tractability of the previously derived multiple Lorentzian model, while being capable of modelling the FBG reflection spectrum over a wider frequency spectrum.

III. UNIFORM FBG DISCRETISED REFLECTION MODEL DERIVATION

We model the reflection response of the uniform FBG as a series partial reflections at boundaries equally spaced over the N layers of the grating. The entire grating has a uniform refractive index n_{eff} , while each boundary has an equal transmission coefficient t and reflection coefficient r at each boundary determined by the normalised refractive index variation $\delta n = \delta n_{eff}/n_{eff}$. Further, we

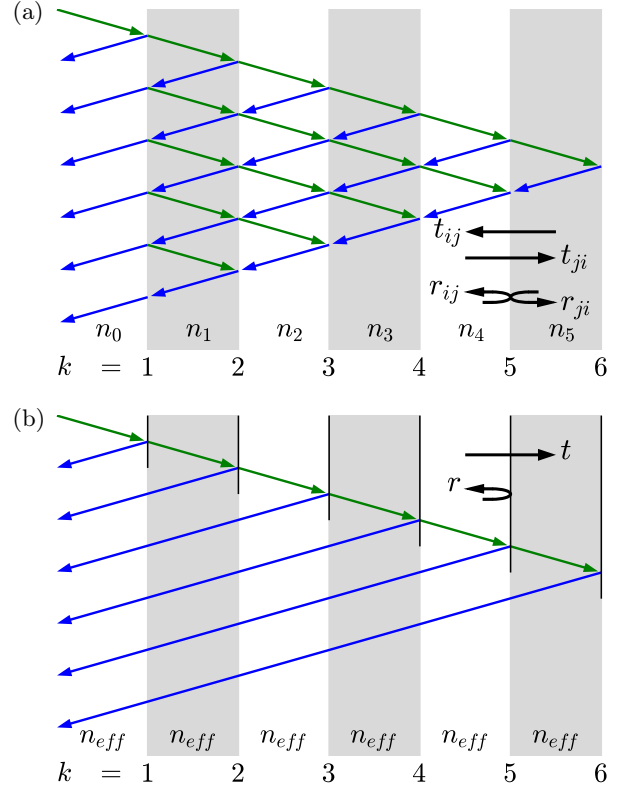


FIG. 4. Illustration of the first 6 layers in the decomposition of an FBG in slabs and the contributions to the total reflected electric field. Each layers' transmission and reflection coefficients are indicated where $j = i + 1$. Illustration of the first 6 layers in the decomposition of an FBG in slabs where only the final contribution due to reflection at the k^{th} is considered for the k^{th} delayed signal. Forward and backward transmission is considered in (a) while only forward transmission is considered in (b).

consider only the dominant paths that undergo a single reflection at the $(k - 1)^{\text{th}}$ layer. Therefore, a single reflection emerges from the uniform FBG after a time delay $\kappa\delta\tau$. For this model to be physically valid, it must accurately reproduce the fundamental characteristics of FBGs — chiefly the total reflectivity R — while ensuring that the introduced parameters r and t have a concrete relationship with the physical parameters of FBGs. With these goals in mind, we begin by rewriting the total reflectivity R in terms of the two key parameters of the discretised model, namely δn and N .

$$R_{\text{exact}} = \tanh\left(\frac{\pi}{2} \frac{N\delta n}{1 + \delta n}\right) \quad (21)$$

The key observation then is that R is approximated very well by

$$R_{\text{approx}} = 1 - (1 - \delta n)^{2N} \quad (22)$$

as shown in Figure 5(a), where both expressions are plotted as a function of δn for different layer numbers N ,

demonstrating the excellent agreement. We now describe two interpretations of this model that produce expressions for r and t which recovers this approximation for R .

A. Discretised reflection interpretation 1: Effective reflectivity

Figure 4(a) illustrates this interpretation of the discretised FBG reflection. At each boundary, a signal propagating forward or backward is either transmitted or reflected. As previously discussed, intra-layer reflections that emerge from the grating after a time delay $k\delta\tau$ are typically grouped together as $h_r(k)$. Here, we approximately account for all intra-layer reflections within $h_r(k)$ through the signal that is reflected at the k^{th} layer, which has an identical time delay. Given that each of these signals are transmitted through $2(k-1)$ layers and reflected once, the reflection coefficient at the k^{th} layer is given by

$$h_r(k) = t^{2(k-1)}r \quad (23)$$

We now require an r and t that recovers (22) when we sum over all reflections $h_r(k)$. Rewriting (22) as a sum,

$$\begin{aligned} R_{\text{approx}} &= 1 - (1 - \delta n)^2 + (1 - \delta n)^2 - \dots \\ &\quad - (1 - \delta n)^{2N-2} + (1 - \delta n)^{2N-2} - (1 - \delta n)^{2N} \\ &= (1 - (1 - \delta n)^2) (1 + (1 - \delta n)^2 + \dots + (1 - \delta n)^{2N-2}) \end{aligned}$$

Therefore,

$$R_{\text{approx}} \equiv \sum_{k=1}^N h_r(k) = (1 - (1 - \delta n)^2) \sum_{k=1}^N (1 - \delta n)^{2(k-1)}$$

which is precisely the desired form for the sum of all reflected signals given by (23) when we define

$$\begin{aligned} t &\equiv 1 - \delta n \\ r &\equiv 1 - t^2 \end{aligned}$$

We therefore have transmission and reflection coefficients t and r for this discretised reflection model which accurately describes the total FBG reflectivity, at least at its Bragg frequency. It is noted that the derived reflection coefficient r , which physically should be larger than what one would derive from optics equations to account for the intra-layer reflections that have been dropped, results in the relation

$$r + t = 1 + \delta n - \delta n^2 > 1 \quad \forall \delta n < 1$$

demonstrating that modelled reflected signals account for many reflected signal, as expected. Although this representation can be used going forward, a slightly different viewpoint on this model produces expressions the authors find preferable.

B. Discretised reflection interpretation 1: Many mirrors

While the previous interpretation 'lives' in the same modelling setup as previous approaches to discretised FBG reflections [57, 58], here we consider a more conceptual model for the FBG which is illustrated in Figure 4(b). We consider the reflected signals emerging from the front facet of the FBG after a time delay $k\delta\tau$ as having effectively passed through $k-1$ partially reflective mirrors in a medium with refractive index n_{eff} before being reflected at the k^{th} , subsequently undergoing no further attenuation. Following this interpretation, the reflected signal at the k^{th} layer has an effective reflection coefficient

$$h_r(k) = t^{k-1}r \quad (24)$$

We now follow the same procedure as done with the previous model, that is calculating r and t that recovers (22) when we sum over all reflections $h_r(k)$. We have that (22) can be written as

$$R_{\text{approx}} = \sum_{k=1}^N h_r(k) = (1 - (1 - \delta n)^2) \sum_{k=1}^N ((1 - \delta n)^2)^{k-1}$$

Then,

$$t \equiv (1 - \delta n)^2 \quad (25)$$

$$r \equiv 1 - t \quad (26)$$

which then has the more preferable property that $r + t = 1$. Given that both interpretations provide identical results, we use these expressions for the effective reflection $h_r(k)$ given by (24) and r and t given by (25).

C. LK equations under discretised FBG reflection

We can, as has been done in several other analyses [41–43, 45, 46], then write the feedback $\eta F(t)$ as the convolution of the electric field with the impulse response

$$\begin{aligned} \eta F(t) &= \eta e^{-iC_p} E(t) \otimes \tilde{\rho}(t) \\ &= \eta e^{-iC_p} E(t) \otimes \sum_{k=0}^{N-1} t^k r \delta(t - \tau - k\delta\tau) e^{-ik\omega_B \delta\tau} \\ &= \eta r e^{-iC_p} \sum_{k=0}^{N-1} t^k E(t) \otimes \delta(t - \tau - k\delta\tau) e^{-ik\omega_B \delta\tau} \\ \eta F(t) &= \eta r e^{-iC_p} \sum_{k=0}^{N-1} t^k E(t - \tau - k\delta\tau) e^{-ik\omega_B \delta\tau} \end{aligned}$$

where $e^{-ik\omega_B \delta\tau}$ accounts for the phase accumulated while propagating through the FBG. This reduces the typical

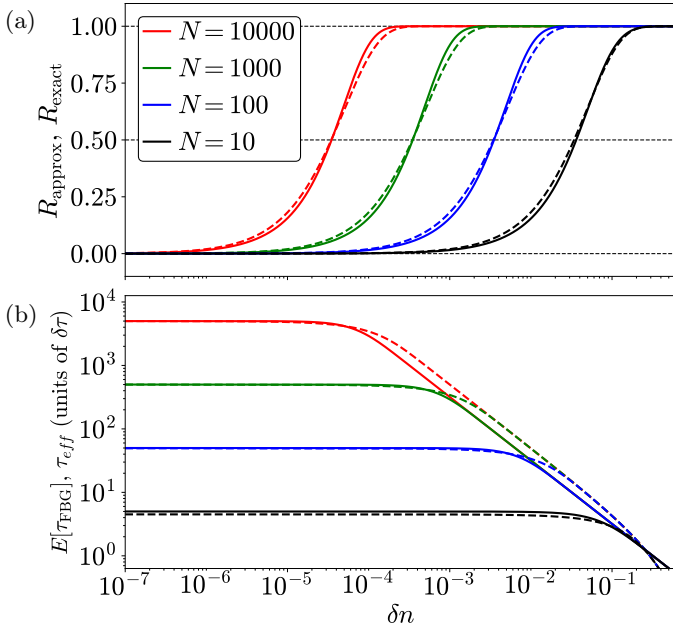


FIG. 5. A comparison between the exact total reflection and discretised total reflection is shown in (a), and the exact effective delay and discretised delay expectation is shown in (b) as functions of the normalised refractive index variation δn for varying $N \in [10, 100, 1000, 10000]$.

integral-based feedback term to a sum of discrete delays, resulting in a form for the LK equations given by

$$\begin{aligned} \frac{dE}{dt} &= (1 + i\alpha)N(t)E(t) + \\ &\quad \eta(1-t)e^{-iC_p} \sum_{k=0}^{N-1} t^k E(t - \tau - k\delta\tau) e^{-ik\omega_B\delta\tau} \\ T \frac{dN}{dt} &= P - N(t) - (1 + 2N(t))|E(t)|^2 \end{aligned} \quad (27)$$

where ω_B measures the grating's detuning from the laser free-running frequency, in the same way as with FOF.

To further justify the physical relevance of these values for t and r in this discretised reflection model, we can, similar to the Lorentzian approximation, compare the expected delay of the discretised reflections to the known effective delay. The effective time delay, given by (??), can be written in terms of the layer round-trip time $\delta\tau = 2\Lambda n_{\text{eff}}/c$ as

$$\tau_{\text{eff}} = \frac{R_{\text{exact}}\delta\tau}{\pi\delta n} \quad (28)$$

The expected delay of the discretised reflections $E[\tau_{\text{FBG}}]$ is calculated as the weighted average of the delays of all the reflected signals, where the weights are the amplitudes of the reflected signals. Mathematically,

$$E[\tau_{\text{FBG}}] = \frac{r \sum_{k=1}^N t^{k-1}(k-1)\delta\tau}{r \sum_{k=1}^N t^{k-1}}$$

The sum in the denominator is simply the sum of a geometric sequence, having a closed form

$$\sum_{k=1}^N t^{k-1} = \frac{1-t^N}{1-t}$$

while the sum in the numerator can be written in terms of a derivative w.r.t. t of the numerator. That is,

$$\sum_{k=1}^N t^{k-1}(k-1) = t \partial_t \sum_{k=1}^N t^{k-1} = \frac{t(1-t^N)}{(1-t)^2} - \frac{Nt^N}{1-t}$$

The effective delay then simplifies to

$$E[\tau_{\text{FBG}}] = \delta\tau \left[\frac{t}{1-t} - \frac{Nt^N}{1-t^N} \right]$$

or alternatively,

$$E[\tau_{\text{FBG}}] = \delta\tau \left[\frac{t}{1-t} - \frac{N(1-R_{\text{approx}})}{R_{\text{approx}}} \right]$$

Figure 5(b) plots both expressions for the total FBG time delay again as function of δn for different layer numbers N . Excellent agreement is seen in the total delay, as was the case with the total FBG reflectivity, particularly for low δn while diverging from the true effective delay as δn increases, further justifying these choices for t and r . We note that this improved agreement in total time delay for lower δn is in direct contrast to the accuracy of the ratio of total reflectivities, which decreases in accuracy as the refractive index change decreases. Given the success of this FBG model in describing both total reflectivity and time delay to a good accuracy, we propose that (27) is a good approximation to the LK equations under FBG feedback, while being amenable to mathematical analyses available to the LK equation under COF. The key derived parameter t , present in (27) is calculated through (22), as

$$t = (1-R)^{\frac{1}{N}} \quad (29)$$

IV. EGM MODES OF THE DISCRETISED REFLECTION MODEL

Given that the derived model is simply a coupled system of DDEs, we can, in the same vein as with ECMs of the COF laser and EFM of the FOF laser, calculate the basic steady-state solutions of the system given by (??). Such solutions are referred to as external grating modes (EGMs) herein. The ability to calculate these modes is a crucial advantage over other systems modelling FBG feedback in semiconductor lasers as they provide much of the understanding in the structure of solutions and their stability [15], while additionally allowing for enhanced model validation with the standard LK equations. Further, once the stable solutions have

been calculated, they can be continued in parameters using specialised DDE numerical continuation software such as `DDE-BifTool`. The EGM modes have the form, where $E_s, \omega_s, N_s \in \mathbb{R}$. These solutions physically correspond to an electric field locked at a frequency ω_s with constant amplitude E_s at a constant inversion N_s . In this form ω_s measures the mismatch from the solitary laser frequency. Inserting this ansatz into (??), one can obtain an implicit equation for the EGM frequencies. We now come to a description of the transition of the EFM-components as the filter detuning D is varied. For $D = 0$ the bulge of the solution envelope is centred at the origin of the (x_s, X) -plane; see Fig. 5(a). The associated single EFM-component is shown in Fig. 6(a). It corresponds to the single, continuous curve in Fig. 7(a). As D is increased, the bulge in the envelope moves along the diagonal towards the top-right of the (x_s, X) -plane; see Fig. 5(b). The EFM-component deforms in the (x_s, N_s) -plane but it is still a single closed curve; see Figs. 6 and 7(b). It surrounds both the frequency of the filter $x_s = D$ and the free-running laser frequency $x_s = X = 0$. As the filter detuning D is increased further, the envelope undergoes a saddle transition T_s at $X = 0$, which can be seen clearly in the Figs. 6(c) and 7(c) as a point where the curve self-intersects. The equations derived for the discretised reflection model very similar to the original LK equations given by (1) in that CW solutions are given by $(E(t), N(t)) = (E_s e^{i\omega_s t}, N_s)$ without additional dimensions introduced by the feedback $F(t)$. We may solve this equation by expanding the complex exponentials into their real and imaginary components,

$$i\omega_s = (1 + i\alpha)N_s + \eta(1 - t)(\cos(\phi_E) - i\sin(\phi_E)) \times \left(\sum_{k=0}^{N-1} t^k \cos(k\phi_F) - i \sum_{k=0}^{N-1} t^k \sin(k\phi_F) \right)$$

where $\phi_F = \delta\tau(\omega_B + \omega_s)$, $\phi_E = C_p + \tau\omega_s$ are distinguished as the phases accrued in the EC and FBG, respectively. In this form, with the aid of identities

$$\begin{aligned} \sum_{k=0}^{N-1} t^k \cos(k\phi_F) &= \frac{1 - t \cos(\phi_F) - t^N \cos(N\phi_F) + t^{N+1} \cos((N-1)\phi_F)}{t^2 - 2t \cos(\phi_F) + 1} \\ \sum_{k=0}^{N-1} t^k \sin(k\phi_F) &= \frac{t \sin(\phi_F) - t^N \sin(N\phi_F) + t^{N+1} \sin((N-1)\phi_F)}{1 - 2t \cos(\phi_F) + t^2} \end{aligned}$$

an implicit equation for the EGM frequencies ω_s can be derived,

$$\omega_s = \frac{\eta(1-t)\sqrt{1+\alpha^2}}{t^2 - 2t \cos(\phi_F) + 1} \times \left[-\sin(\phi_E + \arctan \alpha) + t \sin(\phi_E + \arctan \alpha - \phi_F) + t^N \sin(\phi_E + \arctan \alpha + N\phi_F) - t^{N+1} \sin(\phi_E + \arctan \alpha + (N-1)\phi_F) \right]$$

The RHS can then be written as a single sine function, yielding

$$\omega_s = -\eta(1-t)\sqrt{\alpha^2 + 1} \frac{S_N}{S} \sin(\phi_E + \arctan \alpha + \Phi - \Phi_N) \quad (30)$$

where

$$S = \sqrt{1 - 2t \cos(\phi_F) + t^2} \quad (31)$$

$$S_N = \sqrt{1 - 2t^N \cos(N\phi_F) + t^{2N}} \quad (32)$$

$$\Phi = \arctan \left(\frac{t \sin(\phi_F)}{1 - t \cos(\phi_F)} \right) \quad (33)$$

$$\Phi_N = \arctan \left(\frac{t^N \sin(N\phi_F)}{1 - t^N \cos(N\phi_F)} \right) \quad (34)$$

We note that in the plane mirror limit, the front face of the FBG would reflect all incoming light, that is $t = 0 \implies S = S_N = 1$, $\Phi = \Phi_N = 0$, yielding

$$\omega_s = -\eta\sqrt{\alpha^2 + 1} \sin(C_p + \omega_s \tau + \arctan \alpha)$$

which is precisely the well studied implicit ECM equation [15]. Given the solutions for ω_s , one can calculate N_s and E_s through

$$N_s = -\eta(1-t) \frac{S_N}{S} \cos(\phi_E + \Phi - \Phi_N) \quad (35)$$

$$E_s = \sqrt{\frac{P - N_s}{1 + 2N_s}} \quad (36)$$

The envelope of f is obtained by setting the sine term in (30) to +1 and -1.

$$\omega_s = \mp \eta(1-t)\sqrt{\alpha^2 + 1} \frac{S_N}{S} \quad (37)$$

while a curve of EGMs can also be derived by substituting the CW ansatz into (27).

$$N_s(\omega_s) = \frac{\alpha\omega_s}{1 + \alpha^2} \pm \frac{1}{1 + \alpha^2} \sqrt{-\omega_s^2 + (1 + \alpha^2) \left(\eta(1-t) \frac{S_N}{S} \right)^2} \quad (38)$$

Lastly, while we can directly control the gratings reflectivity and detuning through η (or R), and ω_B , respectively, we can use the number of gratings N to control the FBG bandwidth ω_z through (15) and (29).

$$\omega_z = \omega_c \sqrt{\left(\frac{1 - (1 - R)^{\frac{1}{2N}}}{2}\right)^2 + \frac{1}{N^2}} \quad (39)$$

At this point, we have equations which can visualise the structure of the EGMs predicted by this discretised model which will help to fix the grating reflectivity R and layer number N . We would like to study physically relevant EGMs of FBGs in parameter regions of interest. For 1550 nm light, the lasers angular frequency corresponds to $\omega_c = 1216 \text{ rad ps}^{-1}$. Then, to compare to the Lorentzian model, that nominally had $\omega_z = 0.1$, we must first determine the FBG parameters (ω_B, R, N) in (39). We first prescribe the parameters of the laser and EC to the previously studied values $\tau = 121, \alpha = 3.5, \eta R = 0.0455, C_p = 0, T = 550, P = 0.186$ for COF [9]. It is then important to note that ω_z in the derived form of the LK equations is a dimensionless quantity normalised by the cavity lifetime τ_p , which for these laser parameters is equal to 1.82 ps, see Appendix ?? for details. Therefore, the angular frequency ω_c is nondimensionalised to $\omega_c = 2211$ and then, beginning with a reflectivity $R = 0.5$ the grating number, calculated through (39), is $N \approx 22440$. As was done with the Lorentzian FBG LK model, we visualise EGM frequencies ω_s as intersections of the left- and right-hand sides of (30), defined as $g(\omega_s)$ and $f(\omega_s)$, respectively, and project EGMs in the (ω_s, N_s) -plane. Figure ?? demonstrates excellent agreement in the structure of EGMs within the main lobe of the FBG reflection spectrum with the Lorentzian model. Crucially, in addition to accurately modelling EGMs within the main lobe, potential intersections of side lobes of the reflection spectrum can be seen in (a). Before moving forward with an analysis of EGMs predicted by this model using these initial values of R and N , we discuss two clear issues with the current solution structure. First, in contrast to the Lorentzian model, $f(\omega_s)$ does not precisely equal zero at $\omega_s = \omega_B \pm \omega_z$. These reflection zeros are of particular interest as stability fluctuations around these reflection zeros have been observed and thus including these features in the reflection spectrum is of significance for a physically accurate model. Second and perhaps most pressing is the number of grating layers N , corresponding to that number of additional terms in (27), which is of great significance in numerical simulations. Even for very short gratings $\sim 1 \text{ mm}$, layers have lengths $\sim 0.5 \mu\text{m}$ for 1550 nm light in standard optical fibers, leading to 1000s of delay terms. Although this does not pose any issues when evaluating grating modes and the like with the analytical equations presented thusfar, numerical continuation would immediately be out of reach due to the large computational times associated with a system 1000s of delay terms, while numerical integration would require similar com-

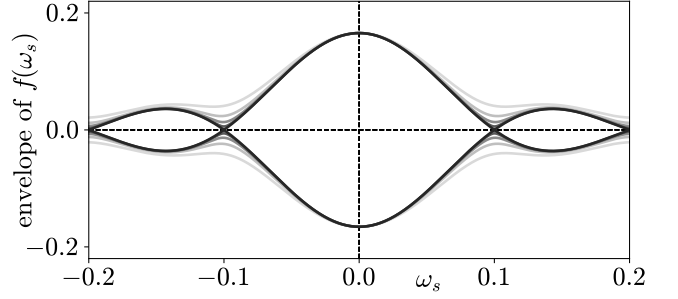


FIG. 6. Variation in the shape of the envelope of $f(\omega_s)$ for $R \in [0.01, 0.2, 0.4, 0.6, 0.8]$ while keeping the effective feedback rate η_{eff} constant.

putational times to that of the convolution or Fourier transform based forms of the feedback term $F(t)$, nullifying many of the advantages that one would seek with the modelling simplifications presented up to now. 1

On the issue of the transmission zeros at $\pm n\omega_z, n \in \mathbb{N}$, we vary the envelope of (30) for varying R , while keeping the total feedback rate ηR constant, as shown in Figure 6. Clearly, the desired transmission zeros are obtained for low values of R . The use of very low values for R does not pose any issues in practice, as one can rescale the feedback rate η so that ηR is at the desired level. We then note that in (15),

$$1 - (1 - R)^{-\frac{1}{2N}} \approx 0, R \ll 1$$

Then, using $\omega_c = 2\pi/\delta\tau$, the location of reflection zeros, given by (39) simplifies to becomes

$$\omega_z \approx \frac{2\pi}{\delta\tau N} \quad (40)$$

This simplification to the location of reflection zeros provides the key to addressing the issue of large number of delays N , which we seek to reduce while still obtaining identical dynamics. This approximation indicates that so long as the product $\delta\tau N$ remains constant, the EGM bandwidth is unchanged. Note that this is equivalent to requiring that the total grating length remains constant, as $L = N\delta\tau c/n_{eff}$. An illustration of this is shown in Figure ???. This tracks with physical intuition on gratings, as very short gratings ($L \ll 1$) act like mirrors, which are like filters with infinite bandwidth, while very long gratings ($L \gg 1$) produce a narrow bandwidth filtering response. We therefore can calculate the required $\delta\tau$ for a desired ω_z and N through (40). The equivalence between different grating numbers is demonstrated in Figure 7, where grating numbers $N \in [10, 22440]$ are used with near identical agreement. We therefore may select a layer number N that is low enough to be amenable to standard numerical analyses such as continuation without encountering significant computational difficulties.

The key difference between using a low grating number is in the number of side lobes that are correctly

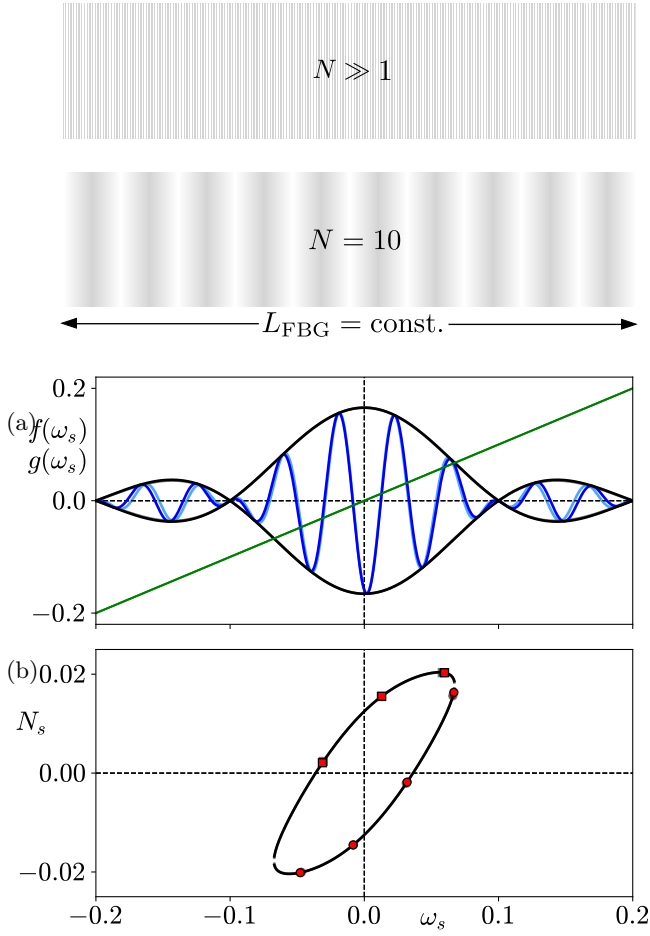


FIG. 7. Illustrations of gratings with equal length but different layer numbers N , each providing near identical reflection zero locations $\omega_B \pm n\omega_z$, $n \in \mathbb{N}$. (b), (c) Equivalence in EGM structure between different grating numbers $N \in [10, 22440]$ by keeping $N\delta\tau$ constant.

modelled. Figure 8 plots the EGM solution curves over $\omega_s \in [-20\omega_z, 20\omega_z]$ for $N = 10$ and $N = 22440$ while keeping $N\delta\tau$ constant. It can be seen that when $N = 10$, a main reflection lobe appears after every $10\omega_z$, meaning that five side lobes are obtained before the model becomes completely non-physical. In contrast, the side lobes continue for the true grating number for 1550 nm light. Overall, a balance must be made between choosing an N that is low enough so that the system is still amenable to analysis through integration and continuation, while not introducing non-physical features to the EGM structure over the parameter region being studied. To this end, we illustrate two undesirable situations that can occur for an insufficiently large N in Figure 9, which plots EGM solutions for $N = 10$ for varying detuning ω_B . The valid solution regions, corresponding to a frequency range of $\pm 5\omega_z$, are plotted with opaque lines while the entire frequency region is plotted with semi-transparent lines. The first case demonstrated in the left column illustrates how if the detuning ω_B becomes

large enough, the valid portion can be completely detuned away from $\omega_s = 0$ as shown in the progression from (a1) to (b1). As the amplitude of side lobes will begin to increase again past this point as shown in (c1) (where they should continue to diminish) one could find larger EGM regions than is physically correct. This can be avoided by ensuring that over the parameter region being studied, N is larger than $2\omega_{B,\max}/\omega_{z,\min}$. The second and perhaps more problematic case shown on the right column, occurs when repeated side lobes intersect the line $f(\omega_s) = \omega_s$, and the repeated main reflection lobes over the entire parameter region of interest. The first repetitions of the main lobe occur at $\omega_s = \pm N\omega_z + \omega_B$, while each main lobe has a maximum at $\pm\eta\sqrt{\alpha^2 + 1}$. The line $f(\omega_s)$ can therefore hit the first repeated main lobes at $\omega_s = \pm\eta\sqrt{\alpha^2 + 1}$. For $\omega_B = 0$ as shown in (a2), only valid regions of the EGM envelope intersect the line $f(\omega_s)$, but as ω_B increases, the first repeated main lobe begins to intersect $f(\omega_s)$ at $\omega_s = \pm\eta\sqrt{\alpha^2 + 1}$ as shown in (b2), introducing invalid EGM components to the solution structure as ω_B is increased as shown in (c2). Note that detuning is not the only mechanism for which this can occur, for example, increasing the feedback rate η in (b1) would increase the amplitude of the solution envelope and quickly cause intersections between the repeated main lobes and $f(\omega_s)$. To guarantee these non-physical features are not introduced into the EGM structure, we therefore require the first repeated peaks to never be within $\omega_s = \pm\eta\sqrt{\alpha^2 + 1}$, which can be ensured through

$$N\omega_z + |\omega_B| > \omega_s = \eta\sqrt{\alpha^2 + 1}$$

Combining these two conditions, a lower bound on the grating number N for a particular parameter region can then be prescribed as

$$N_{\min} = \begin{cases} \left\lceil \frac{2|\omega_B|_{\max}}{\omega_{z,\min}} \right\rceil, & |\omega_B|_{\max} > \eta_{\max}\sqrt{1 + \alpha_{\max}^2} \\ \left\lceil \frac{|\omega_B|_{\max} + \eta_{\max}\sqrt{1 + \alpha_{\max}^2}}{\omega_{z,\min}} \right\rceil, & \text{otherwise} \end{cases} \quad (41)$$

Note then, that the final grating parameter $\delta\tau$, which determines the grating length L , controls the grating bandwidth. The effective feedback rate is defined as $\eta_{eff} \equiv \eta R$. We can now compare the two derived models describing FBG distributed feedback. The first of which derived directly from the FBG reflection spectrum $\rho(\omega)$ using Lorentzian distributions, and the present model, approximating the FBG impulse response $\tilde{\rho}(t)$. We compare EGM solutions of both models using identical parameters in Figure ?? where results obtained by the discretised reflections model are plotted with solid lines and round markers, while results obtained by the Lorentzian model are plotted with dashed lines and square markers. Remarkable agreement between these models can be seen, in spite of their independent derivations. The nulls

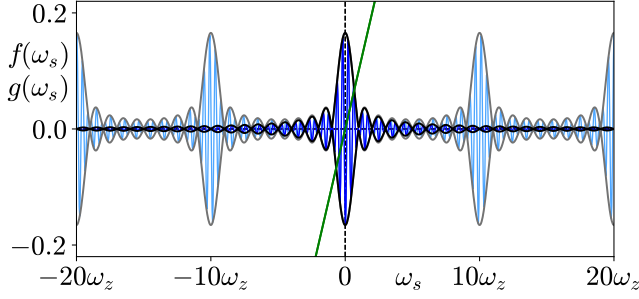


FIG. 8. EGM solutions over a wide frequency range $\omega_s \in [-20\omega_z, 20\omega_z]$ for two different grating numbers $N = 10$ and $N = 22440$ while keeping $N\delta\tau$ constant.

of the envelopes of $f(\omega_s)$ in both cases agree precisely, while their values at $\omega_s = 0$ only show slight disagreement, due to the error in total reflectivity in the discretised reflection model for $R = 0.01$. Further, both models predict 11 EGMs with excellent agreement in their locations. As the Lorentzian model has a more physically concrete derivation, this gives strong evidence as to the physical relevance of the discretised reflection model, while having the added benefit of modelling side lobes of the reflection spectrum.

V. COMPARISON TO PREVIOUSLY STUDIED FBG FEEDBACK MODELS

Given the excellent agreement in ECMs confined to the main lobe between the three Lorentzian model and the discretised reflection model, we now compare agreement in solution structure and system dynamics between the discretised reflection model and the various approaches to modelling the feedback term $F(t)$ within the LK equations in the literature. This section demonstrates the excellent agreement this discretised model demonstrates with significantly less computational effort, while portraying several analysis techniques available to this system that is not possible with previously studied forms of FBG feedback.

A. EGM Accuracy

A considerably more complex system presented by Naumenko *et al.* in [53] considers the feedback term $F(t)$ in the form of (2) that is, as the inverse Fourier transform of the product of the time delayed electric field in the spectral domain $\mathcal{F}[E(t - \tau)](\omega)$ and the grating reflection spectrum $\rho(\omega)$. The model additionally considers nonlinear gain and frequency chirp due to thermal effects when the injection current is changed. Ignoring these additional effects, and making suitable approximations, the system simplifies to the derived discretised reflection system as shown in Appendix C with parameter values

$(\alpha, P, T, \tau, C_p) = (4, 0.5, 123, 512, 0)$, and varying grating parameters η , ω_B , and ω_z .

EGMs were calculated with the help of Green functions through an involved mathematical procedure, as opposed to deriving closed form analytical equations. As discussed in the introduction, they identified ‘satellite’ EGMs, separated from the central EGM envelope by the zeros of the main lobe by varying both grating bandwidth ω_z and detuning ω_B . Figure 10 compare results obtained by both the multiple EC reflection FBG feedback and discretised FBG models for varying grating reflectivity, bandwidth and detuning. In order to obtain valid EGM solutions, for both parameter sets, $N = 10 > N_{\min} = 7$ was used. Solutions are projected in the frequency-intensity plane where $I = |E|^2$, in contrast to the usual projection in the inversion-frequency plane, causing an inversion of the cavity modes about the frequency axis. The photon lifetime $\tau_p = 24$ ps was used to convert grating bandwidths in Hz to their nondimensionalised ω_z form. Clearly, excellent agreement in the mode structure is achieved, in particular for the low feedback rate case. Firstly, considering no detuning, low feedback and varying bandwidths as is the case in Figure 10, for a wide bandwidth of the Bragg reflector (in this case, a main lobe width of $40/3$ GHz or $2\omega_z = 0.64\pi$ in nondimensionalised form), EGMs lie on a closed curve, resembling a COF ECM structure, as expected. The MGM (mode with highest power) is located for near the edge of the left side of the closed curve, indicated by an ‘x’ in the figure. As the FBG bandwidth is decreased, the number of EGMs decreases, and the EGM solution curve and MGM narrows as they are confined to within the bandwidth of the main lobe, in agreement with results obtained from Sections ?? and IV and with results obtained for a single Lorentzian filter [28]. Further narrowing the filter bandwidth introduces satellite EGMs, indicated with triangles, due to the side lobes of the FBG reflection spectrum. It is noted that this effect does not occur in the single Lorentzian filter for zero detuning. At this point, the MGM is nearly at the Bragg frequency, in agreement with physical intuition. Increasing the feedback rate considerably, and detuning the FBG from the laser’s free-running frequency, as shown in Figure ??, also detune the EGM modes, and split the modes into three disjoint curves, corresponding to the main lobe and two side lobes nearest to the laser’s free-running frequency. This splitting of solution curves was similarly observed for the single Lorentzian filter [28], but at most two disjoint curves can be formed [11], while in this case already three distinct solution curves are present. Significant distortion in the EGM structure along the intensity axis can be seen for the discretised reflection case compared to the Multiple EC reflection model, which can be attributed to the lack of a gain suppression factor in this model in this simplified model. In any case, excellent agreement in the locations of the EGM components, MGM, and number of EGM solutions demonstrates the ability of the discretised reflections model to capture the solution structure

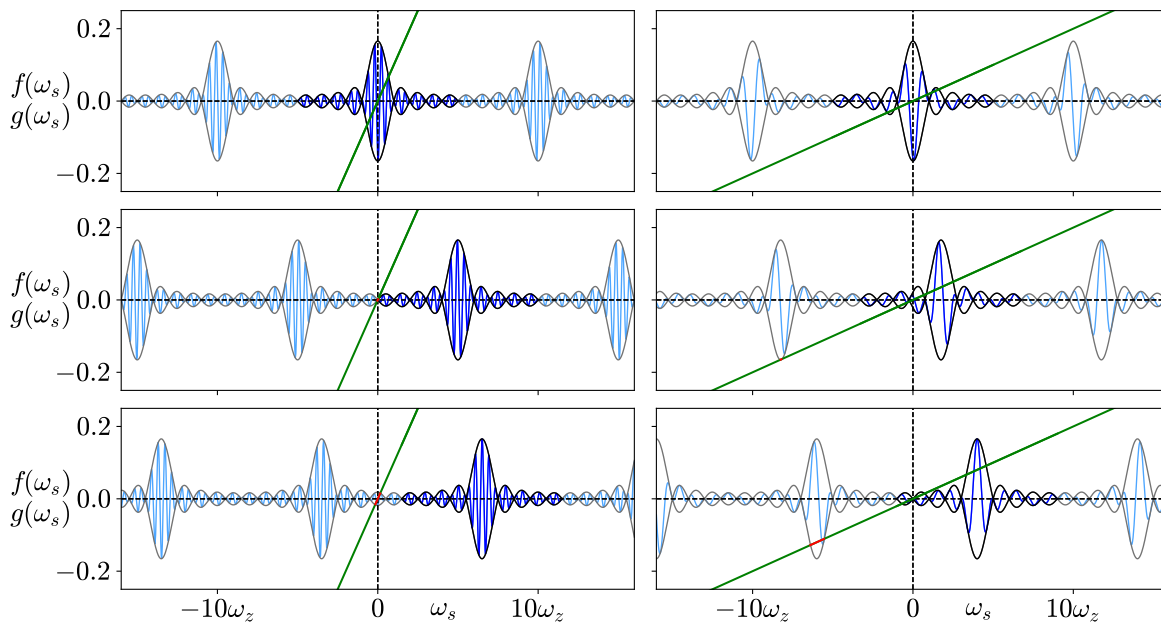


FIG. 9. EGM solutions for varying detuning ω_B with $\omega_z = 0.1$ (left) and $\omega_z = 0.02$ (right) and $N = 10$ in both cases. Valid region solution regions are plotted with opaque lines while the entire frequency region is plotted with semi transparent lines.

of FBG feedback.

B. Stability Fluctuations

It is important to note that while the locations of zeros in the discretised model are uniform, is only the case for FBGs which have relatively low reflectivities, see Figure 2. For this, re

Finally, we compare our model to the most recent work on semiconductor lasers under FBG feedback by Skönderas *et al.* [45, 46]. In contrast to the previous two models, where nondimensionalisations and approximations were required before direct comparisons could be made, the form of the equations analysed mirror the equations presented in this work, using parameter values $(\alpha, P, T, \tau) = (3, 1, 1000, 1000)$, except for the use of a convolution feedback term $F(t)$ of the form (19). The results presented by Skönderas *et al.* therefore serve as the most suitable basis for comparisons in the accuracy of the derived discretised model. Given the complexity of analysing the LK equations under FBG feedback using a convolution term, the results presented, like those previously studied, are obtained solely through analysis of time series obtained through numerical integration. The main focus of their analysis is in characterising the interplay between the lasers relaxation oscillations (ROs) and the FBG reflection zeros as a function of feedback rate η and grating bandwidth ω_z for varying feedback phase C_p and grating detuning ω_B .

ROs are the most typical type of oscillation that one would expect in semiconductor lasers. They are damped intensity fluctuations that occur when the laser tran-

sitions between steady states, typically after a sudden change in injection current, and arise from the dynamic interplay between photon density and carrier density in the laser cavity. When the carrier population is perturbed, it overshoots the steady-state value, causing oscillations in output power at a characteristic frequency known as the relaxation oscillation frequency $\omega_{RO} = \sqrt{2P/T}$, which form the dominant side lobes either side of the centre frequency in the Fourier spectrum of a semiconductor laser. Exciting the ROs of a laser can lead to a more unstable laser, and therefore one would expect that lower amount of feedback would cause the laser to transition from steady output to oscillatory and then more unstable outputs.

The strategy employed by the authors to observe this behaviour is by tracking the Hopf bifurcation of the steady state of the laser in the (L_{FBG}, η) -plane, where the grating length L_{FBG} can be used to control the grating bandwidth ω_z as discussed in IV. As discussed in ??, varying the grating length also changes the grating reflectivity, therefore, when using this model, grating parameters must be simultaneously varied to solely vary its bandwidth. This is not an issue with the discretised reflections model as bandwidth ω_z and thus length L_{FBG} can be varied independent of reflectivity using 40

$$L[\text{m}] \approx \frac{\pi c \tau_p}{\omega_z n_{\text{eff}}} \quad (42)$$

where τ_p is the photon lifetime used to rescale time in this form of the LK equations as discussed in Section IV.

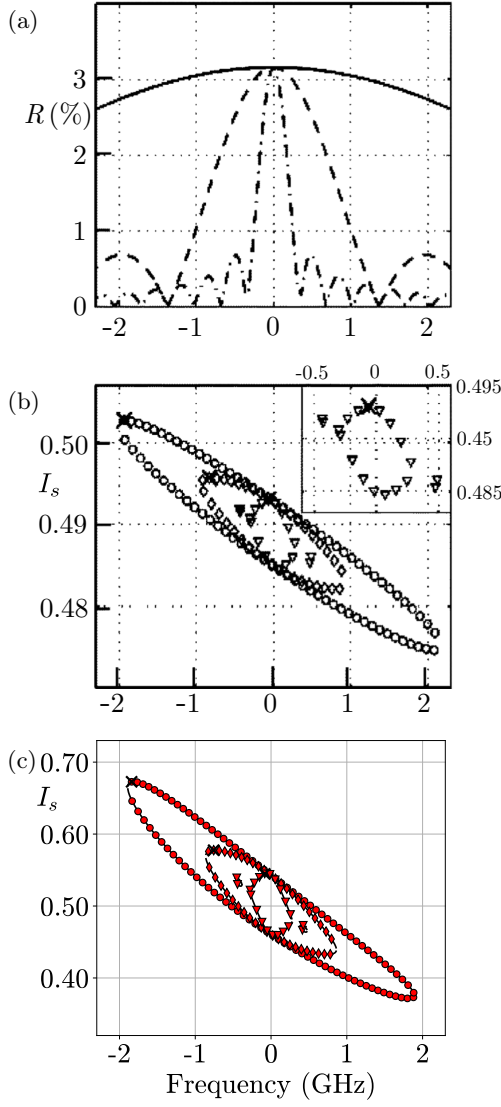


FIG. 10. A comparison between EGMs in the multiple reflection (left) and discretised FBG (right) models in the frequency-intensity domain for varying grating bandwidth and zero detuning. The curves in panels (a1) and (a2) illustrate the FBG frequency responses. A constant reflectivity of $R = 0.0316$ yields a nondimensionalised effective feedback rate $\eta = 0.085$ while Bragg grating reflection zeros at $1/3$, $4/3$, and $20/3$ GHz yield nondimensionalised reflection zero locations $\omega_z = 0.016\pi$, 0.064π , 0.32π . The EGMs in panels (b1) and (b2) corresponding to these respective bandwidths are plotted with circles (\circ), diamonds (\diamond) and squares (\square), while the MGM in each case is plotted indicated by a \times .

CONCLUSIONS AND FUTURE DEVELOPMENTS

While a low reflectivity R does provide the desired transmission zeros, the relative errors in both total reflectivity R_{error} and delay τ_{error} are larger compared to larger total reflectivities. This is demonstrated in Figure 15, which visualises the combined relative errors R_{error} and

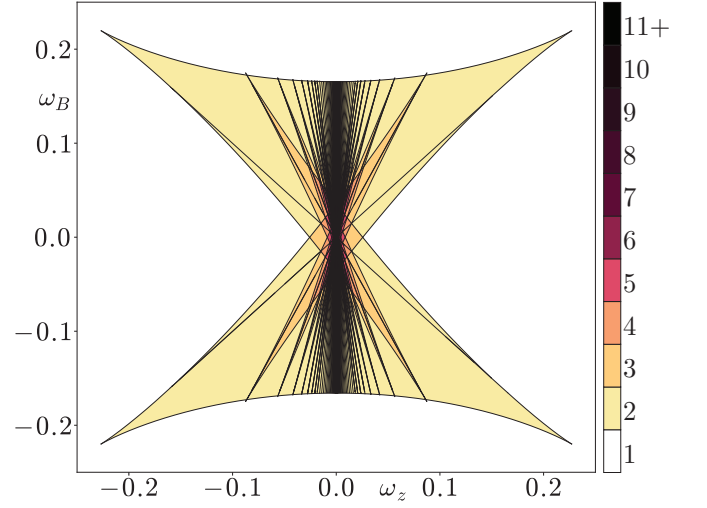


FIG. 11. Caption.

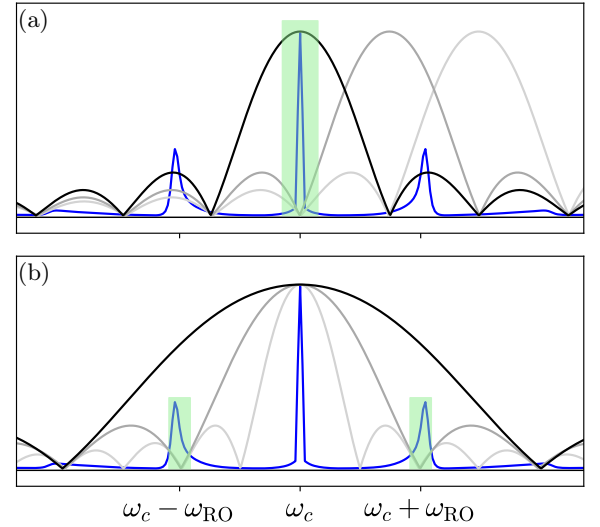


FIG. 12. Caption

τ_{error} using the Euclidean metric $\|R_{\text{error}}, \tau_{\text{error}}\|_2 = \sqrt{R_{\text{error}}^2 + \tau_{\text{error}}^2}$. For the choice $N = 10$, a total reflectivity $R_{\text{approx}} = 0.75$ would provide a lower combined error of 4% as shown in (a) compared to the $R_{\text{approx}} = 0.1$ which has a combined error of 19%. As the ability to effectively describe and analyse transmission zeros of FBGs is of great interest, this increase in combined error, which is still relatively low from a modelling perspective, is an acceptable trade-off.

ACKNOWLEDGMENTS

We acknowledge ...

Appendix A: Nondimensionalisation of the original LK Equations

To model the dynamics of a semiconductor laser with optical feedback from an external cavity, we use the well-known **Lang-Kobayashi equations** [8]. These delay differential equations describe how the complex electric field E of the laser and the carrier inversion N evolve in time under the influence of both intrinsic gain mechanisms and delayed feedback. In dimensionalised form, the equations are written as:

$$\begin{aligned}\frac{dE}{ds} &= \frac{1}{2}G_{M0}(1+i\alpha)[N-N_N]E + \kappa_0 e^{-iC_p} F(s, \tau_0) \\ \frac{dN}{ds} &= J_0 - \gamma_0 N - [\Gamma_{M0} + G_{N0}(N-N_N)]|E|^2.\end{aligned}\quad (A1)$$

The physical parameters in these equations are defined as follows:

- α : linewidth enhancement factor
- γ_0 : carrier decay rate
- Γ_{M0} : cavity decay rate
- κ_0 : feedback strength
- τ_0 : external round-trip delay
- G_{M0}, G_{N0} : small-signal gain coefficients
- J_0 : pump current
- N_N : inversion at threshold

To simplify the equations and reduce the number of parameters, we introduce scaled variables:

$$X = \frac{G_{M0}}{2\gamma_p}(N - N_N), \quad A = \sqrt{\frac{G_{N0}}{2\gamma_0}}E,$$

where $\gamma_p = \Gamma_{M0}G_{M0}/G_{N0}$ is a rescaled photon lifetime. Rescaling time via $t = \gamma_p s$, the Lang-Kobayashi equations become:

$$\begin{aligned}\frac{dA}{dt} &= (1+i\alpha)AX + \eta e^{-iC_p} F(t, \tau) \\ T \frac{dX}{dt} &= P - X - (1+2X)|A|^2\end{aligned}$$

The transformed parameters are defined as:

- $P = \frac{G_{M0}}{2\gamma_p\gamma_0}(J_0 - \gamma_0 N_N)$: pumping rate above threshold
- $T = \frac{\gamma_p}{\gamma_0}$: ratio of photon to carrier lifetime
- $\eta = \frac{\kappa_0 G_{N0}}{G_{M0}\Gamma_{M0}}$: normalized feedback strength
- $\tau = \gamma_p \tau_0$: rescaled external delay

For example, dimensionalised parameter values $\alpha = 3.5$, $\gamma_0 = 1.0 \times 10^9$, $\Gamma_{M0} = 0.55 \times 10^9$, $\kappa_0 = 25.0 \times 10^9$, $\tau_0 = 0.22 \times 10^{-9}$, $G_{M0} = 50.0$, $G_{N0} = 0.05$, $J_0 = 8.0 \times 10^9$, $N_N = 5.0$ result in $\gamma_p = 5.5 \times 10^{11}$ and nondimensionalised parameter values $\alpha = 3.5$, $P = 0.136$, $T = 550$, $\eta = 0.0455$, $\tau = 121$. It is noted that one can get from this nondimensionalised time to seconds by multiplying by the factor $\tau_p = 1/\gamma_p = 1.82 \times 10^{-12}$ s.

Appendix B: Convolution FBG LK model equivalence

The form of the equations analysed by Li *et. al* [41–43] are given by

$$\begin{cases} \frac{da}{dt} = \frac{1-ib}{2} \left[\frac{\gamma_c \gamma_n}{\gamma_s \tilde{J}} \tilde{n} - \gamma_p (|a|^2 - 1) \right] a \\ \quad + \gamma_c \xi_f e^{i\theta} [r(t) e^{-i\Delta\Omega t}] * a(t - \tau_{RT}) \\ \frac{d\tilde{n}}{dt} = -(\gamma_s + \gamma_n |a|^2) \tilde{n} - \gamma_s \tilde{J} \left(1 - \frac{\gamma_p}{\gamma_c} |a|^2 \right) (|a|^2 - 1) \end{cases} \quad (B1)$$

we first make a change of notation:

$$\begin{cases} a = E \\ \tilde{n} = N \\ F(t) = [r(t) e^{-i\Delta\Omega t}] * a(t - \tau_{RT}) \\ t = s \end{cases}$$

Resulting in

$$\begin{cases} \frac{dE}{ds} = \frac{1-ib}{2} \left[\frac{\gamma_c \gamma_n}{\gamma_s \tilde{J}} N - \gamma_p (|E|^2 - 1) \right] E + \gamma_c \xi_f e^{i\theta} F(s) \\ \frac{dN}{ds} = -(\gamma_s + \gamma_n |E|^2) N - \gamma_s \tilde{J} \left(1 - \frac{\gamma_p}{\gamma_c} |E|^2 \right) (|E|^2 - 1) \end{cases}$$

Focusing on the first equation, we use:

$$\frac{\gamma_n \gamma_c}{\gamma_s \tilde{J}} \gg \gamma_p$$

to obtain:

$$\frac{dE}{ds} \approx \frac{1}{2} \frac{\gamma_n \gamma_c}{\gamma_s \tilde{J}} (1-ib) N E + \gamma_c \xi_f e^{i\theta} F(s)$$

Then, for the second equation,

$$\begin{aligned}\frac{dN}{ds} &= -\gamma_s N - \gamma_n |E|^2 N - \gamma_s \tilde{J} |E|^2 + \frac{\gamma_s \gamma_p \tilde{J}}{\gamma_c} |E|^4 \\ &\quad + \gamma_s \tilde{J} - \frac{\gamma_s \gamma_p \tilde{J}}{\gamma_c} |E|^2 \\ &= \gamma_s \tilde{J} - \gamma_s N - \left[\gamma_s \tilde{J} \left(1 + \frac{\gamma_p}{\gamma_c} \right) + \gamma_n N \right] |E|^2 + \frac{\gamma_s \gamma_p \tilde{J}}{\gamma_c} |E|^4\end{aligned}$$

Neglecting the $|E|^4$ term, the system can therefore be written as:

$$\begin{cases} \frac{dE}{ds} = \frac{1}{2} \frac{\gamma_n \gamma_c}{\gamma_s \tilde{J}} (1-ib) N E + \gamma_c \xi_f e^{i\theta} F(s) \\ \frac{dN}{ds} = \gamma_s \tilde{J} - \gamma_s N - \left[\gamma_s \tilde{J} \left(1 + \frac{\gamma_p}{\gamma_c} \right) + \gamma_n N \right] |E|^2 \end{cases}$$

which is precisely the form of (A1) for

$$b = -\alpha, \quad \theta = -C_p, \quad G_{M0} = \frac{\gamma_n}{\gamma_s \tilde{J}}, \quad \kappa_0 = \gamma_c \xi_f,$$

$$J_0 = \gamma_s \tilde{J}, \quad \gamma_0 = \gamma_s, \quad \Gamma_{M0} = \gamma_s \tilde{J} \left(1 + \frac{\gamma_p}{\gamma_c} \right), \quad G_{N0} = \gamma_n$$

Appendix C: Multiple EC reflection FBG LK model conversion

The form of the LK equations studied by Naumenko *et al.* [53, 54] is given by

$$\begin{cases} \frac{dE}{dt} = \left[\frac{1}{2} \Gamma G_N \{ i\alpha (N - N_{th}) + g(N, I) \} \right. \\ \quad \left. - \frac{1}{2\tau_\mu} + \frac{1}{\tau_{in}} \ln \left(\frac{\bar{F}(t)}{E} \right) + i\Delta\omega_0 \right] E \\ \frac{dN}{dt} = \frac{I}{eV} - \frac{N}{\tau_N(N)} - G_N g(N, I) I \end{cases} \quad (C1)$$

where $g(N, I)$ is the nonlinear gain, $N/\tau_N(N)$ is the spontaneous emission rate, $\Delta\omega_0$ is the frequency chirp due to thermal effects when the injection current is changed, and,

$$\bar{F}(t) = E + \frac{(-1)}{2\pi} \frac{(1 - r_2^2)}{r_2^2} \sum_{n=1}^{\infty} e^{-i\omega_0 n \tau} \times \int_{-\infty}^{+\infty} d\omega (-r_2 r_B(\omega))^n e^{i\omega(t - n\tau)} \int_{-\infty}^{+\infty} dt' E(t') e^{i\omega t'} \quad (C2)$$

Assuming a negligible gain compression factor and thermal frequency detuning (by setting $\epsilon \approx 0$ and $k = 0$, respectively, following the expressions in [53]), and linearising the spontaneous emission rate, these equations can be rewritten as

$$\begin{cases} \frac{dE}{dt} = \frac{1}{2} \Gamma G_N (1 + i\alpha) (N - N_{th}) E + \frac{1}{\tau_{in}} \ln \left(\frac{\bar{F}(t)}{E} \right) E \\ \frac{dN}{dt} = \frac{J - \bar{J}_0}{eV} - \frac{N}{\tau_0} - \left[\frac{1}{\Gamma \tau_{ph}} + G_N (N - N_{th}) \right] |E|^2 \end{cases}$$

Now, rescaling time by $t = \tau_{in} s$, one obtains

$$\begin{cases} \frac{dE}{ds} = \frac{1}{2} \tau_{in} \Gamma G_N (1 + i\alpha) (N - N_{th}) E + \ln \left(\frac{\bar{F}(s)}{E} \right) E \\ \frac{dN}{ds} = \frac{\tau_{in} (J - \bar{J}_0)}{eV} - \frac{\tau_{in}}{\tau_e} N - \left[\frac{\tau_{in}}{\Gamma \tau_{ph}} + G_N \tau_{in} (N - N_{th}) \right] |E|^2 \end{cases}$$

Which is precisely the form (A1) when replacing the multiple EC reflection term $E \ln (\bar{F}(s)/E)$ with

$\kappa_{0,eff} e^{-iC_p} F(s)$ for

$$\alpha = \alpha, \quad N_N = N_{th}, \quad G_{M0} = \tau_{in} \Gamma G_N, \quad G_{N0} = G_N \tau_{in}$$

$$J_0 = \frac{\tau_{in} (J - \bar{J}_0)}{eV}, \quad \gamma_0 = \frac{\tau_{in}}{\tau_e}, \quad \Gamma_{N0} = \frac{\tau_{in}}{\Gamma \tau_{ph}}, \quad \tau_0 = \frac{2L_{ext} n_{ext}}{c \tau_{in}}$$

where:

$$\tau_{ph} = \frac{1}{c\alpha_{in}/n_g - 1/\tau_{in} \ln(R_1 R_2)} \text{ and } N_{th} = N_0 + \frac{1}{\Gamma G_N \tau_{ph}}$$

$\kappa_0 = \kappa_{0,eff} R$ can be determined by reducing the multiple EC reflection feedback term as a single reflection,

$$E \ln \left(\frac{\bar{F}(s)}{E} \right) \stackrel{n=1}{\approx} \frac{1 - R_2^2}{R_2} e^{-iC_p} \mathcal{F}^{-1} [\rho(\omega) \mathcal{F} [E(s - \tau_0)](\omega)](s)$$

which is precisely in our notation

$$E \ln \left(\frac{\bar{F}(s)}{E} \right) = \frac{1 - R_2^2}{R_2} e^{-iC_p} F(s)$$

Therefore, in the single reflection case:

$$\kappa_0 = \frac{1 - R_2^2}{R_2} R$$

Then, we can convert to the non-dimensionalised model following the transformations in Appendix A.

Appendix D: Derivation of Variational equations for the Discretised reflection FBG LK Equations

Beginning with the discretised reflections model, consisting of the complex valued electric field variable E and real valued carrier density variable N .

$$\dot{E} = (1 + i\alpha) N E + \eta(1 - t) e^{-iC_p} \sum_{k=0}^{N-1} t^k e^{-i\omega_B \delta \tau} E(t - \tau_k)$$

$$\dot{N} = \frac{1}{T} [P - N - (1 + 2N)|E|^2]$$

The variational equations are defined as

$$\frac{d}{dt} \begin{pmatrix} \delta E \\ \delta N \end{pmatrix} = \mathbf{J}(\underline{F}) \begin{pmatrix} \delta E \\ \delta N \end{pmatrix} + \sum_{k=1}^N \mathbf{J}_{\tau_k}(\underline{F}) \begin{pmatrix} \delta E_{\tau_k} \\ \delta N_{\tau_k} \end{pmatrix} \quad (D1)$$

where $\underline{F}(t) = (\dot{E}(t), \dot{N}(t))^T$, which results in

$$\begin{aligned} \delta \dot{E}(t) &= (1 + i\alpha) [\delta E N + E \delta N] \\ &\quad + \eta(1 - t) e^{-iC_p} \sum_{k=0}^{N-1} t^k e^{-i\omega_B \delta \tau} \delta E(t - \tau_k) \end{aligned} \quad (D2)$$

$$\delta \dot{N}(t) = -\frac{1}{T} [2(1 + 2N) \text{Re} \{ \bar{E} \delta E \} + (1 + 2|E|^2) \delta N]$$

- [1] V. Heiskanen and M. R. Hamblin, *Photochemical & Photobiological Sciences* **17**, 1003 (2018).
- [2] G. Van Tartwijk and D. Lenstra, *Quantum and Semi-classical Optics: Journal of the European Optical Society Part B* **7**, 87 (1995).
- [3] C. O. Weiss and R. Vilaseca, *NASA STI/Recon Technical Report A* **92**, 39875 (1991).
- [4] R. Tkach and A. Chraplyvy, *Journal of Lightwave technology* **4**, 1655 (2003).
- [5] A. Uchida, K. Amano, M. Inoue, K. Hirano, S. Naito, H. Someya, I. Oowada, T. Kurashige, M. Shiki, S. Yoshimori, *et al.*, *Nature Photonics* **2**, 728 (2008).
- [6] G. Stépán, *Retarded dynamical systems: stability and characteristic functions* (1989).
- [7] M. C. Mackey and L. Glass, *Science* **197**, 287 (1977).
- [8] R. Lang and K. Kobayashi, *IEEE journal of Quantum Electronics* **16**, 347 (1980).
- [9] T. Heil, I. Fischer, W. Elsässer, B. Krauskopf, K. Green, and A. Gavrielides, *Physical Review E* **67**, 066214 (2003).
- [10] A. M. Yacomotti, L. Furfaro, X. Hachair, F. Pedaci, M. Giudici, J. Tredicce, J. Javaloyes, S. Balle, E. A. Viktorov, and P. Mandel, *Physical Review A—Atomic, Molecular, and Optical Physics* **69**, 053816 (2004).
- [11] K. Green and B. Krauskopf, *Optics communications* **258**, 243 (2006).
- [12] T. Heil, I. Fischer, and W. Elsässer, *Physical Review A* **58**, R2672 (1998).
- [13] S. Wieczorek, B. Krauskopf, and D. Lenstra, *Optics communications* **172**, 279 (1999).
- [14] S. Wieczorek, B. Krauskopf, T. B. Simpson, and D. Lenstra, *Physics Reports* **416**, 1 (2005).
- [15] V. Rottschäfer and B. Krauskopf, *International Journal of Bifurcation and Chaos* **17**, 1575 (2007).
- [16] J. Sieber, K. Engelborghs, T. Luzyanina, G. Samaey, and D. Roose, *arXiv preprint arXiv:1406.7144* (2014).
- [17] B. Krauskopf, K. Green, H. Erzgräber, and D. Lenstra, in *Semiconductor Lasers and Laser Dynamics*, Vol. 5452 (SPIE, 2004) pp. 82–92.
- [18] B. Krauskopf, G. R. Gray, and D. Lenstra, *Physical Review E* **58**, 7190 (1998).
- [19] K. Green and B. Krauskopf, *Optics communications* **231**, 383 (2004).
- [20] B. Krauskopf and K. Green, in *Physics and Simulation of Optoelectronic Devices X*, Vol. 4646 (SPIE, 2002) pp. 453–462.
- [21] T. Erneux, A. Gavrielides, K. Green, and B. Krauskopf, *Physical Review E* **68**, 066205 (2003).
- [22] K. Green and B. Krauskopf, *Physical Review E* **66**, 016220 (2002).
- [23] D. H. DeTienne, G. R. Gray, G. P. Agrawal, and D. Lenstra, *IEEE journal of quantum electronics* **33**, 838 (1997).
- [24] B. Dahmani, L. Hollberg, and R. Drullinger, *Optics letters* **12**, 876 (1987).
- [25] K. Harvey and C. Myatt, *Optics letters* **16**, 910 (1991).
- [26] S. Jin, Y. Li, and M. Xiao, *Applied optics* **35**, 1436 (1996).
- [27] G. Agrawal, *IEEE Journal of Quantum Electronics* **20**, 468 (1984).
- [28] M. Yousefi and D. Lenstra, *IEEE Journal of Quantum Electronics* **35**, 970 (1999).
- [29] H. Erzgräber, B. Krauskopf, D. Lenstra, A. Fischer, and G. Vemuri, *Physical Review E—Statistical, Nonlinear, and Soft Matter Physics* **73**, 055201 (2006).
- [30] H. Erzgräber, B. Krauskopf, and D. Lenstra, *SIAM Journal on Applied Dynamical Systems* **6**, 1 (2007).
- [31] H. Erzgräber and B. Krauskopf, *Optics letters* **32**, 2441 (2007).
- [32] A. P. Fischer, O. K. Andersen, M. Yousefi, S. Stolte, and D. Lenstra, *IEEE journal of quantum electronics* **36**, 375 (2000).
- [33] A. Fischer, M. Yousefi, D. Lenstra, M. W. Carter, and G. Vemuri, *IEEE Journal of selected topics in quantum electronics* **10**, 944 (2004).
- [34] G. Hek and V. Rottschäfer, *IMA journal of applied mathematics* **72**, 420 (2007).
- [35] H. Erzgräber, D. Lenstra, B. Krauskopf, A. Fischer, and G. Vemuri, *Physical Review E—Statistical, Nonlinear, and Soft Matter Physics* **76**, 026212 (2007).
- [36] A. P. Fischer, M. Yousefi, D. Lenstra, M. W. Carter, and G. Vemuri, *Physical review letters* **92**, 023901 (2004).
- [37] M. Yousefi, D. Lenstra, G. Vemuri, and A. P. Fischer, in *Proceedings of the Annual Symposium IEEE-LEOS Benelux Chapter* (2001) pp. 41–44.
- [38] M. Yousefi, D. Lenstra, G. Vemuri, and A. P. Fischer, in *Physics and simulation of optoelectronic devices X*, Vol. 4646 (SPIE, 2002) pp. 447–452.
- [39] M. Yousefi, D. Lenstra, and G. Vemuri, *Physical Review E* **67**, 046213 (2003).
- [40] T. Erdogan, *Journal of lightwave technology* **15**, 1277 (1997).
- [41] S.-S. Li, Q. Liu, and S.-C. Chan, *IEEE Photonics Journal* **4**, 1930 (2012).
- [42] S.-S. Li and S.-C. Chan, *IEEE Journal of Selected Topics in Quantum Electronics* **21**, 541 (2015).
- [43] S.-S. Li, X. Zou, L. Wang, A. Wang, W. Pan, and L. Yan, *Optics Express* **28**, 21286 (2020).
- [44] P. Jiang, P. Zhou, N. Li, P. Mu, and X. Li, *Optics Express* **29**, 17815 (2021).
- [45] M. Skönderas, N. Gupta, S. W. Jolly, T. Geernaert, and M. Virte, in *Laser Science* (Optica Publishing Group, 2021) pp. JT1A–10.
- [46] M. Skönderas, S. W. Jolly, N. Gupta, T. Geernaert, and M. Virte, *Optics Letters* **47**, 1602 (2024).
- [47] V. Annovazzi-Lodi, G. Aromataris, M. Benedetti, and S. Merlo, *IEEE Journal of Quantum Electronics* **44**, 1089 (2008).
- [48] D. Rontani, A. Locquet, M. Sciamanna, and D. Citrin, *Optics letters* **32**, 2960 (2007).
- [49] D. Wang, L. Wang, T. Zhao, H. Gao, Y. Wang, X. Chen, and A. Wang, *Optics Express* **25**, 10911 (2017).
- [50] D. Wang, L. Wang, Y. Guo, Y. Wang, and A. Wang, *Optics Express* **27**, 3065 (2019).
- [51] D.-M. Wang, Y.-H. Lei, P.-F. Shi, and Z.-A. Li, *Chinese Physics B* **32**, 090505 (2023).
- [52] M. Chao, D. Wang, L. Wang, Y. Sun, H. Han, Y. Guo, Z. Jia, Y. Wang, and A. Wang, *Optics Communications* **456**, 124702 (2020).
- [53] A. Naumenko, P. Besnard, N. Loiko, G. Ughetto, and J. Bertreux, *IEEE Journal of Quantum Electronics* **39**, 1216 (2003).

- [54] A. Naumenko, N. A. Loiko, C. Guignard, and P. Besnard, in *Laser Optics 2003: Diode Lasers and Telecommunication Systems*, Vol. 5480 (SPIE, 2004) pp. 11–19.
- [55] P. Besnard, A. Naumenko, N. A. Loiko, G. Ughetto, and J. Bertreux, in *ICONO 2001: Nonlinear Optical Phenomena and Nonlinear Dynamics of Optical Systems*, Vol. 4751 (SPIE, 2002) pp. 577–588.
- [56] H. Rong-Qing and T. Shang-Ping, IEEE Journal of Quantum Electronics **25**, 1580 (1989).
- [57] J. Capmany, M. A. Muriel, and S. Sales, Optics letters **32**, 2312 (2007).
- [58] F. Ghiringhelli and M. N. Zervas, Physical Review E **65**, 036604 (2002).

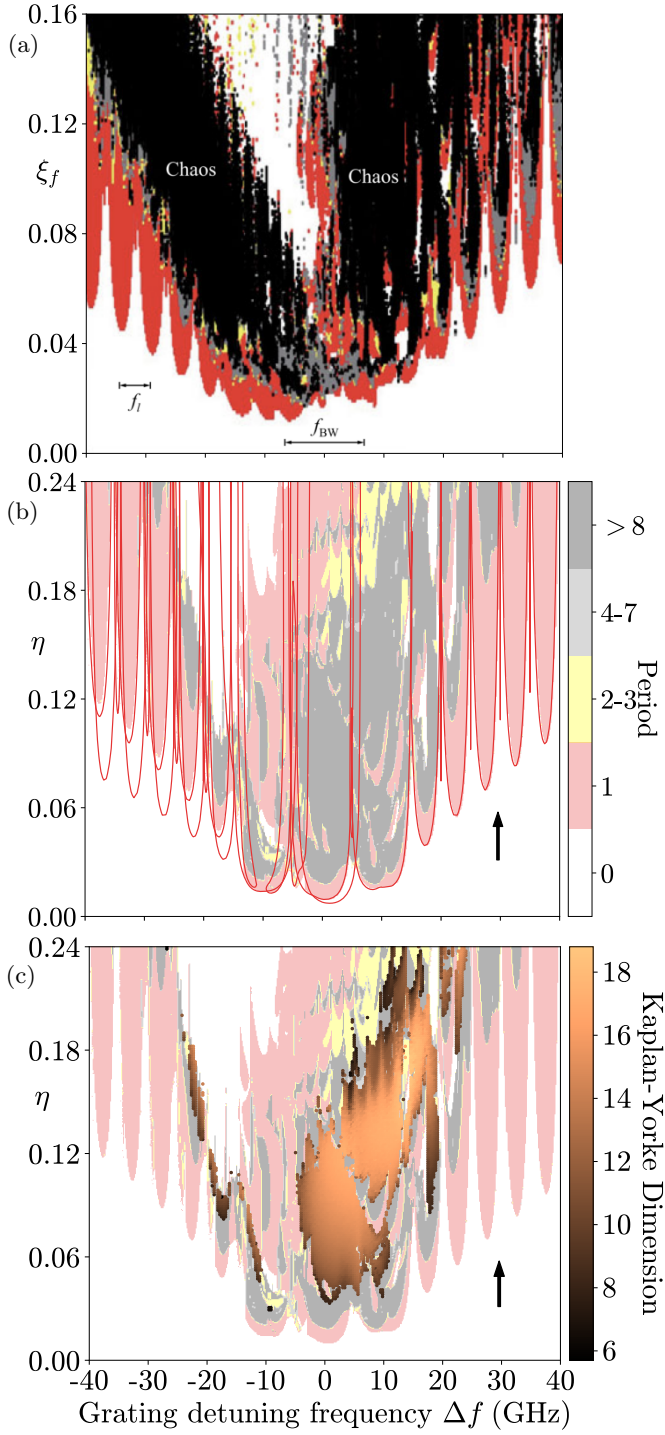


FIG. 13. Comparison between two parameter dynamical mappings of output intensity for a convolved FBG feedback form of $F(t)$ [41–43] (a) and the discretised FBG feedback form of $F(t)$ in the parameter space of feedback strength (ξ_f in (a) and equivalent η in (b)) and grating detuning frequency (Δf). In (a), the laser output intensity is stable (white), period-one oscillatory (red), quasi-periodic pulsating (gray), period-doubled oscillatory (yellow), and chaotic (black). In (b), the laser output is in steady-state (white), period-one oscillatory (red), period-two (yellow), and period 3 to very large period in a gradient from grey to black. In (c) parameter sweeps are performed in all four directions, with Hopf bifurcations of steady state EGMs overlayed.

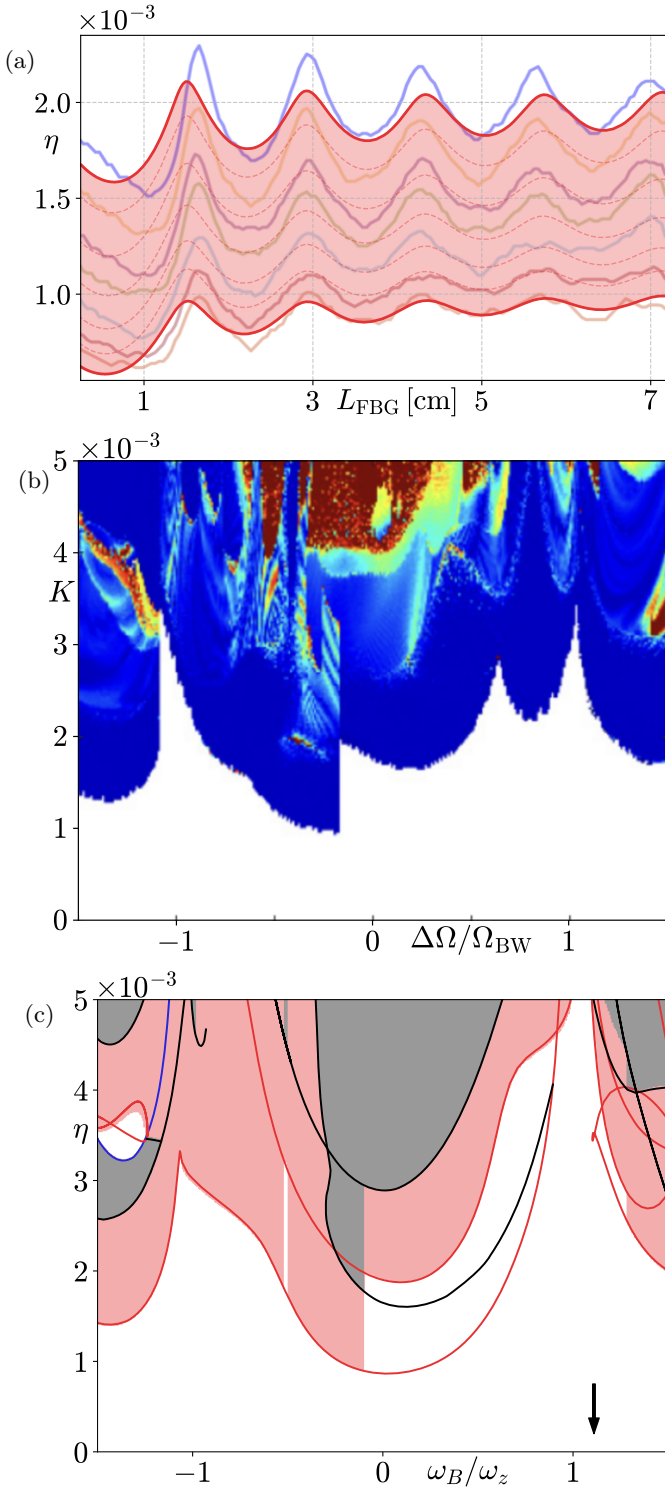


FIG. 14. The evolution of Hopf bifurcation tracking the stability fluctuations as a function of L_{FBG} at zero detuning for different values of the feedback offset phase C_p equal to 0 (blue), $\pi/4$ (yellow), $\pi/2$ (violet), $2\pi/3$ (green), π (cyan), $3\pi/2$ (maroon), and $7\pi/4$ (orange). Comparison between two parameter dynamical mappings of output intensity for a convolved FBG feedback form of $F(t)$ [41–43] (a) and the discretised FBG feedback form of $F(t)$ in the parameter space of feedback strength (ξ_f in (a) and equivalent η in (b)) and grating detuning frequency (Δf). In (a), the laser output intensity is stable (white), period-one oscillatory (red), quasi-periodic pulsating (gray), period-doubled oscillatory (yellow), and chaotic (black). In (b), the laser output is in steady-state (white), period-one oscillatory (red), period-two (yellow), and period 3 to very large period in a gradient from grey to black. In (c) parameter sweeps are performed in all four directions,

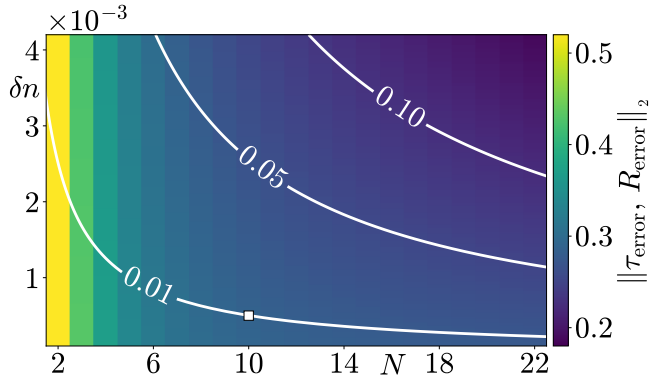


FIG. 15. Combined relative errors of FBG total reflectivity R_{error} and delay τ_{error} as a function of the grating number N and normalised refractive index variation δn . Level sets of constant total reflectivity R_{approx} are overlayed in white. In (a), the square marker at $(N, \delta n) = (10, 0.07)$, corresponding to an $R_{\text{approx}} = 0.75$ has a combined error of 4% while in (b), the marker at $(N, \delta n) = (10, 0.0055)$, corresponding to an $R_{\text{approx}} = 0.1$ has a combined error of 19%.